Chiral spintronics

See-Hun Yang[1] ✉, *Ron Naaman*[2], *Yossi Paltiel*[3] *and Stuart S. P. Parkin*[4] ✉

Abstract | As spins move through a chiral electric field, the resulting spin current can acquire chirality through a spin–orbit interaction. Such spin currents are highly useful in creating spin–orbit torques that can be used to manipulate chiral topological magnetic excitations, for example, chiral magnetic domain walls or skyrmions. When the chiral domain walls form composite domain walls, via an antiferromagnetic exchange coupling, novel phenomena, including an exchange coupling torque and domain wall drag, are observed. Here, we review recent progress in the generation and functionalities of spin currents derived from or acting on chiral structures. By bringing together advances in chiral molecules, chiral magnetic structures and chiral topological matter, we provide an outlook towards potential applications.

Chirality is a broken symmetry of an object in either real or reciprocal space, with which the chiral object does not overlap with itself after a reflection or inversion operation. Such operations are fundamentally distinct from rotations or translations. Remarkably, moving spins can couple to a chiral object via a spin–orbit interaction. Spin currents that are related to chirality are often more efficient than their achiral counterparts, thereby, reducing energy consumption, and making chiral spintronics a fast-moving field with much research focused on searching for new chiral materials and devices with novel functionalities. For example, it has been found that large spin currents can be generated from chiral molecules, chiral topological insulators (TIs) and chiral Weyl semimetals. In addition, it has been discovered that chiral spin–orbit torque (SOT) can move chiral domain walls and chiral skyrmions very efficiently. Hence, we believe that it is timely to review the remarkable progress in chiral spintronics over the past decade.

In this Review, we discuss three types of chiral spintronics. The first two deal with real-space phenomena, namely, chiral systems that produce chiral spin currents, such as chiral molecules, and spin currents that influence chiral systems, such as chiral magnetic domain walls and skyrmions. The third type includes reciprocal-space-induced chiral spin currents, which occur in chiral topological materials. These chiral spin currents are dissipationless, making them of particular interest for reducing energy consumption. Although these topics appear to be disconnected at first glance, the underlying physics and, in particular, their origin are common. Thus, by bridging these distinct topics, knowledge and know-how developed independently can be interchanged and intertwined, accelerating progress in these fields. For example, large spin currents derived from chiral topological materials[1] and chiral spin currents from chiral molecules[2] can both be used to efficiently drive chiral magnetic structures.

Chirality, helicity and handedness

Chirality plays a critical role in a wide range of systems, from biology and chemistry to condensed matter physics and high energy physics. For example, in the biochemistry and pharmaceutical industries, enantiomer separation is a major issue, since enantiomers with a specific chirality often have different biochemical properties or pharmacological effects from their counterparts with the opposite chirality[3]. However, there are subtle differences in the definition of chirality, depending on the discipline. In particle physics, chirality is an abstract concept that is defined from Lorentz group transformations. In this Review, what is relevant is, rather, the projection of the spin on the direction of motion, otherwise known as helicity. The helicity is defined by the relative orientation between a moving spin and its velocity, so that, when they are parallel (antiparallel), the helicity is right-handed (left-handed). For massless particles, the helicity is invariant under a Lorentz transformation, since these particles travel at the speed of light, which cannot be exceeded in any inertial reference frame and, consequently, the helicity is well defined. However, when the particles are massive, there exists an inertial frame in which an observer can move faster than the spin, which cannot move faster than light. In the observer's frame, the helicity would be switched, since the velocity direction changes in that frame. Hence, the helicity is not Lorentz invariant for massive particles. Chirality was introduced to define a Lorentz-invariant quantity, even for massive particles. Consequently, the helicity is not the same as the chirality for massive particles, whereas these quantities are identical for massless particles. Thus, chirality is the more general quantity. Since we mostly deal

[1]*IBM Research – Almaden, San Jose, CA, USA.*
[2]*Weizmann Institute of Science, Rehovot, Israel.*
[3]*The Hebrew University of Jerusalem, Jerusalem, Israel.*
[4]*Max Planck Institute, Halle, Germany.*
✉*e-mail: seeyang@us.ibm.com; stuart.parkin@mpi-halle.mpg.de*

https://doi.org/10.1038/s42254-021-00302-9

Key points

- When a spin travels through a chiral structure in which the reflection or inversion symmetry is broken, the moving spin can be polarized, thereby giving rise to spin currents. The key ingredient to produce such spin currents is spin–orbit interaction.
- The spin currents are central to the chiral spintronics. The chiral structures that generate the spin currents can be found not only in a real space but in a reciprocal space.
- The exemplary chiral structures in the real space are chiral molecules, chiral magnetic domain walls and chiral skyrmions, while what can be found in the reciprocal space are chiral topological materials.
- Chiral spintronics deals with not only the generation of the spin currents but the acting of spin currents on chiral structures, such as chiral spin–orbit torque.
- The spin currents from chiral structures such as chiral molecules and chiral topological materials can often be significantly larger than the achiral counterparts. Reversely, the spin currents acting on chiral structures, such as chiral spin–orbit torque, is much more efficient than achiral spin transfer torque.
- Chiral spintronics based on chiral magnetic structures are particularly useful for the potential development of devices that have better performances and new functionalities.

with spins moving at the Fermi velocity ($\sim 10^6$ m s^{-1}) in condensed matter physics, it is assumed that the chirality is the same as the helicity. In chemistry and biology, the chirality corresponds to the geometrical handedness. In this Review, we adopt the definitions of handedness and chirality that are commonly used in biology and chemistry when dealing with chiral molecules.

Chiral-induced spin selectivity. In general, as a spin moves transverse to an electric field, the spin becomes chiral, owing to the spin–orbit interaction (SOI). Therefore, we expect that a chiral potential will differentiate between spins moving in opposite directions. Chirality breaks the symmetry, since a specific spin is favoured, depending on the momentum and electric field directions. The spin polarization, electric field and momentum are each orthogonal to each other from relativistic effects. Since the handedness of a chiral object determines the relative orientation of the geometrical path of the spin with respect to the electric field, the spins become polarized. This effect is termed chiral-induced spin selectivity (CISS)[4]. The CISS effect is proportional to the length of the chiral molecule: a spin polarization of as much as 20% is typically observed over a distance of just 1 nm (REF.[5]).

There are a number of conditions that can amplify the spin filtering and detection processes. The scattering matrix of spins at contacts with the chiral molecules should be non-unitary, so that the number of spins into and out of these contacts is not conserved. The energies of the spins are complex numbers that rely on the spin directions. Consequently, the spin decay lengths depend on the spin orientation, thereby, effectively increasing the spin polarization. This contact effect can significantly amplify the magnitude of the CISS. To detect CISS experimentally, a nonlinear I–V characteristic is needed, especially for a two-terminal magnetoresistance measurement of the CISS effect. Since the SOI does not break time-reversal symmetry, the Onsager reciprocal relation does not allow for the detection of two-terminal charge signals in the linear response regime at low bias voltage. Hence, nonlinearity in I–V curves is required to probe the CISS in a two-terminal setup[6–8]. Note that the nonlinearity is induced by the energy-dependent electron transport and energy relaxation due to inelastic processes[9,10]. Specific spin orientations can be filtered out using spin relaxation and spin-flip processes at the contacts. Spins spiralling along chiral molecules with different handedness are shown schematically in FIG. 1a. Note that the electric field points in an outward radial direction, so as to confine the spins.

Chiral spin–orbit torque. An electrical current can be used to switch the magnetization of a system through a mechanism called spin transfer torque (STT). Generally, this conventional STT is a symmetric process. However, when a moving spin interacts with chiral magnetic nanostructures, such as chiral magnetic domain walls and skyrmions, chiral SOTs arise from an interplay of different effects — the Dzyaloshinskii–Moriya antisymmetric exchange interaction (DMI)[11,12], the Rashba effect[13] and the spin Hall effect[14].

The DMI occurs in structures with broken inversion symmetry, such as at an interface between a heavy metal (platinum or tungsten) and a magnetic layer that exhibits perpendicular magnetic anisotropy. Such an interface can generate an effective electric field perpendicular to the plane of the interface, due to the difference in work functions between the neighbouring materials. This gives rise, in the reference frame of the spin, to an effective magnetic field that is asymmetric with respect to spin's momentum — the Rashba effect. Consequently, when spins travel along the interface, they become polarized and generate a spin current similar to the case of chiral molecules. The spin Hall effect occurs in materials with strong SOI. When an external bias is applied, spin currents are formed around the edge of the sample. There are two major contributions to this effect: an extrinsic contribution, which is derived from scattering, for example, from impurities, and an intrinsic contribution, which is derived from Berry curvature effects. The direction of the chiral SOT is determined by the directions of the spin Hall effect, the Rashba effect and the DMI. Note that the DMI induces an effective local magnetic field that sets up a specific chirality of the magnetic texture. The DMI can be used for other purposes, such as field-free SOT switching of magnetization[15], formation of static synthetic skyrmions[15], and the injection and inversion of chiral domain walls that are critical to the development of domain wall logic devices[16–18].

When the SOT acts on a composite domain wall that is formed from two chiral domain walls via antiferromagnetic exchange coupling across a thin spacer layer such as Ru, more interesting phenomena can be observed[19,20]. For example, the composite domain wall is displaced very fast by a novel exchange coupling torque (ECT) that is proportional in strength to the strength of the antiferromagnetic exchange. This ECT increases in strength as the net magnetization of the composite domain wall is reduced[19]. If the exchange coupling is weak but still locks the two domain walls, and the current-induced torque on one domain wall is significantly larger than the other, the chirality of the magnetization of the latter domain wall oscillates and

the velocity of the composite domain wall dramatically slows down to zero[20].

Chirality in momentum space. In momentum space, chiral spin currents are induced along surfaces due to broken reflection or inversion symmetry. This is the case for topological materials. As for the case of chiral molecules, the spins are locked to the spin's momentum, but the induced spin currents can be dissipationless[21], thereby, allowing the development of highly efficient spintronic devices. When time-reversal symmetry is broken by magnetic order or impurities in TIs, chiral spin currents form along the 1D edges, rather than at the 2D surfaces[22]. These chiral spin currents give rise to exotic phases such as quantum anomalous Hall insulators, axion insulators and Chern insulators, thus, providing additional knobs to develop novel spintronic devices with new functionalities. Another class of topological materials, Dirac and Weyl semimetals[23], in which topological Dirac and Weyl cones in the interior and Fermi arcs at the surface of the Brillouin zone, respectively, may induce even larger charge-to-spin current conversion ratios than in TIs. Therefore, these emerging materials have unique properties that make them very exciting for the field of chiral spintronics and especially for potential applications.

Chiral-molecule-based spintronics

Spin filtering is commonly associated with magnetic materials or substances that possess large spin–orbit coupling, rather than with organic molecules that are typically non-magnetic. However, various chiral organic molecules and biomolecules have been shown to act as spin filters[24–26] through the mechanism of CISS[4]. CISS requires a system with SOI that polarizes moving spins in the presence of an electric field transverse to the spin's momentum. This means that a right-handed spin travels through right-handed chiral molecules more easily than left-handed spins, and vice versa. Consequently, the incoming spins become polarized depending on the handedness of chiral molecules, such that the transmission through the molecule is spin-selective[4]. CISS-based switching of magnetic systems via chiral-molecule-generated spin currents can be very efficient at room temperature[24], allowing for the possibility of low-power devices[5,27,28].

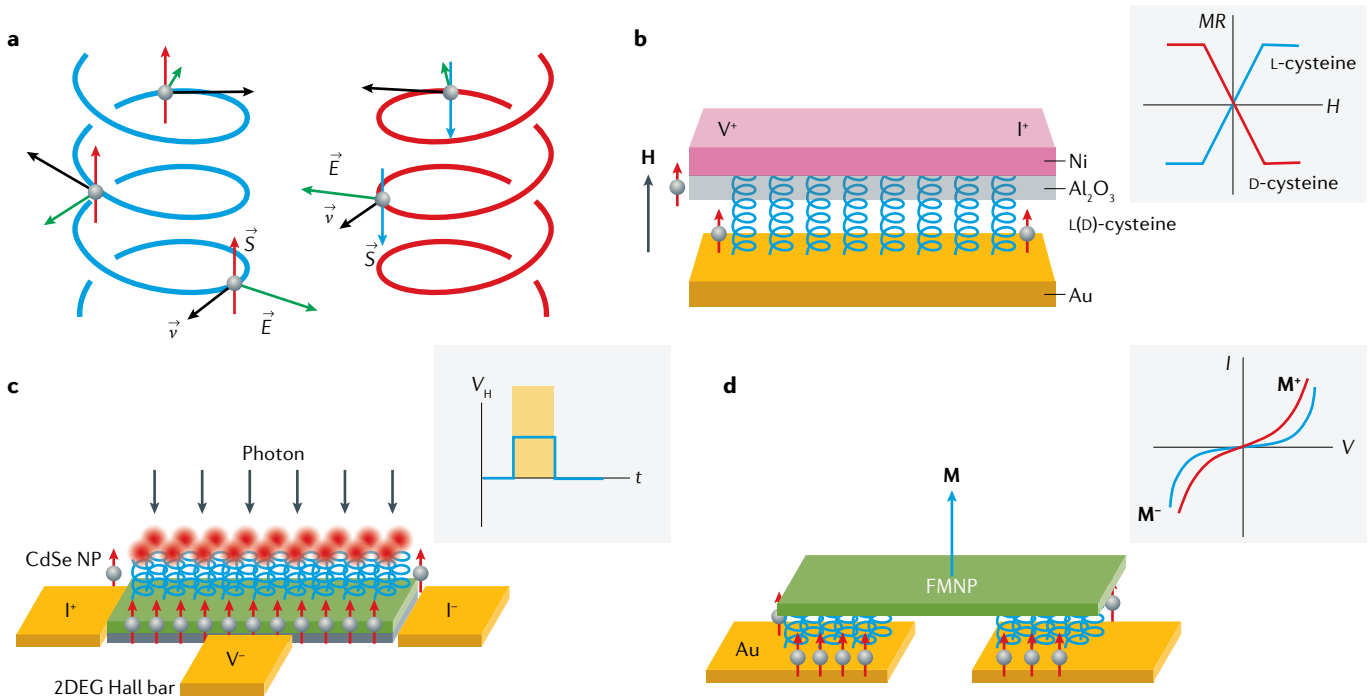

Fig. 1 | **Chiral-molecule-based spintronics. a** | Schematic of spins spiralling along chiral molecules with different handedness. Note that the electric field points in an outward radial direction, so as to confine the spins. **b** | Spin valve with Al_2O_3 deposited on top of chiral molecules consisting of D-cysteine and L-cysteine (with different chiralities) on a gold surface[42]. The spin injector transmits only one spin orientation, independent of the external magnetic field. Inset shows the magnetoresistance (*MR*) measured with a magnetic field (*H*), which depends on the handedness of the chiral molecules that act as a spin filter. **c** | Field-free Hall effect from nanoparticles (NPs) formed from CdSe that are attached to the substrate mediated by chiral molecules (oligopeptides) that are adsorbed on top of the conductive channel formed within a 2D electron gas (2DEG) at the AlGaN/GaN (REF.[48]). Photoexcitation of the NPs induces an exciton, as an electron with a specific spin is transmitted from the substrate to the hole on the NP, leaving an unpaired electron in the substrate. The excited electron in the NP is transmitted back to the substrate, leading to a net spin polarization in the substrate and production of an effective magnetic field, which induces a field-free Hall effect. Inset shows the Hall voltage in the response to the laser irradiation pulse as a function of time. **d** | I–V curve depending on magnetization direction from the device that consists of chiral molecules (AHPA) that are adsorbed on the Au contact using thiolated linkers, and ferromagnetic nanoparticles (FMNP) using the carboxylate end of the chiral linkers[53]. For the case of AHPA-L, when current flows, up spins are injected into the FMNP, while down spins are extracted from the FMNP. In this case, the Au ferromagnetic contacts are in the high resistance state, while the FMNP junctions are in the low resistance state. I–V characteristic curve depends on the handedness of the chiral molecules and the magnetization direction owing to a chiral-induced spin selectivity effect.

While CISS has attracted much attention, the mechanism that gives rise to CISS is not yet fully understood, although certain conditions amplify the process, as discussed previously. Most theoretical studies[29–35] model the coupling of the electron spin direction and velocity to the helical geometry of a molecule using scattering-matrix or tight-binding methods. While the SOI alone is too weak to account for the CISS effect, the combination of SOI with dipole electric fields, and a spin exchange interaction with donor groups or the substrate, can lead to strong, spin-dependent transmission at room temperature[36].

A common approach in spintronics is to use magnetic materials that allow for the control and/or detection of the spins. Spintronic devices that are based on the CISS, however, do not need permanent magnets[37]. Devices utilizing CISS are typically made of self-assembled monolayers of chiral molecules[36] and single chiral molecules[38]. Examples of significant spin filtering include a high spin-filtering efficiency of 80% that was observed for poly-T wrapped single-walled carbon nanotubes[39], a 86% spin filtering from 2D chiral hybrid lead-iodide perovskites[40] and an 88% spin-dependent electron transfer rate between quantum dots in chiral quantum dot assemblies[41].

Spin valves. A CISS-based spin valve consists of a non-magnetic substrate on which chiral molecules are adsorbed[37,42] (FIG. 1b). The adsorbed chiral molecules are coated with a thin oxide layer and a ferromagnetic layer. The coupling between semiconductor quantum dots, or between an organic die to a ferromagnetic substrate, is changed using links formed from chiral molecules[43]. Thus, absorption of light selects one magnetization over the other. Since the chiral molecules transmit spins with specific orientations via a CISS effect, the ferromagnetic layer acts as a spin detector, such that the device responds asymmetrically with respect to the orientation of the magnetic moment that can be switched by an applied magnetic field. Thus, the resistance is high in one field direction and low in the other, which is correlated with the handedness of the chiral molecules and spin and momentum directions. In experiments, typically, a single monolayer of chiral molecules is self-assembled, on top of which a thin film of Al_2O_3 is grown. The Al_2O_3 film adapts a chiral structure that is induced by the underlying self-assembled chiral monolayer. High spin selectivity can be obtained when the self-assembled chiral monolayer is formed from chiral molecules such as cysteine, thus, displaying asymmetric magnetoresistance as a function of field. The sign of the slope is shown to depend on the chirality of the molecules[42]. Spins ejected from the device are polarized either parallel or antiparallel to the spin momenta, which can be useful for devices with perpendicularly magnetized layers.

Hall sensors. Light irradiation or thermal treatments can switch the direction of the spin polarization by incorporating artificial molecules[28]. The device utilizes the chirality inversion of molecular motors as a light-driven, reconfigurable spin filter owing to CISS. Hall-type memory devices or sensors based on CISS do not require permanent charge currents with large signal-to-noise ratios and can be based on semiconductors[44]. Unlike two-terminal devices (like the spin valve), the off state has low noise level and a current is not needed to measure the Hall voltage[45]. Magnetization can be induced by an electric field using chiral molecules. This was demonstrated by using either a GaAs/AlGaAs (REF.[46]) or GaN/AlGaN (REF.[47]) heterostructure that hosts a 2D electron gas and is coated with self-assembled monolayers of chiral molecules (FIG. 1c). In GaAs/AlGaAs devices, localized magnetic fields were observed from a submicron-scale device at room temperature by applying a small gate voltage (~0.1 V). Spin injection by CISS from chiral molecules into the semiconductor magnetizes surface impurity states, which is enhanced by the 2D electron gas. Here, the magnetic moment orientation can be switched by low gate voltages at megahertz rates. The measured Hall response shows that the induced magnetic fields are in the region of hundreds of oersteds and the response of the induced magnetization is faster than 1 MHz, thus, allowing manipulation of induced magnetization at high frequency with good signal-to-noise ratios[45]. Although the response speed is much slower than for conventional semiconductor-based Hall sensors, this is, nevertheless, a significant improvement in chiral-molecule-based devices, which are typically very slow.

This device can be used, for example, to probe the organization of self-assembled α-helix peptide monolayers and to investigate the correlation between structures and spin transfer phenomena[48]. Detection of the temperature dependent structure of self-assembled α-helix peptide monolayers looks like a cold denaturation process in peptides, but, in this case, the self-assembled monolayer plays a role as a solvent. The structural change results in a flip of the electrical dipole moment in the adsorbed molecules that is accompanied by a concomitant change in spin selection as the spins travel through the molecules. This can be probed by a conventional Hall sensor that does not need an external magnetic field or magnetic materials.

The CISS has been recently observed from enantioselective intensity in cross-polarization magic-angle-spinning nuclear magnetic resonance in amino acid enantiomers, while the chemical shift for all nuclei involved remains unchanged. This indicates that the CISS-induced spin polarization affects the nuclear relaxation time (T1) by modifying the molecular magnetic environment[49]. It has also been reported that the photoinduced CISS from a chiral 2D hybrid organic–inorganic perovskite can induce an additional magnetic moment at the interface of an organic perovskite with a Ni–Fe layer that is detected by the magneto-optical Kerr effect[50]. The spin current generated by the CISS can be probed via an inverse spin Hall effect that converts spin current into charge current. For example, an inverse spin Hall voltage was observed from the monoaxial chiral dichalcogenide $CrNb_3S_6$ interfaced with a tungsten layer, with the observation that the Hall voltage had opposite signs for opposite chiralities of the $CrNb_3S_6$ (REF.[51]).

Scaling down devices. To reduce the CISS device size, a continuous ferromagnetic layer can be replaced by single-domain ferromagnetic nanoplatelets. Studies show that ~30-nm-diameter ferromagnetic nanoplatelets are large enough to function as memory devices. Clear dual magnetization behaviour is observed with a threefold change in conductance between on and off states[52] (FIG. 1d). The CISS device behaves like a nonlinear memristor operating at low voltage under ambient conditions and room temperature. Here, even a single nanoparticle, along with Au contacts and chiral molecules, can function as a soft magnet in a memory device, and ferromagnetic nanoplatelets can be used as a fixed reference magnet combined with Au contacts[53].

The asymmetric adsorption of chiral molecules onto paramagnetic nanostructures can stabilize a ferromagnetic state even in very small structures, thus, allowing further scaling down of CISS devices[54]. It has been shown that the CISS effect can stabilize a ferromagnetic state from iron oxide nanoparticles, with an average coercive field of a hundred oersteds. The moment orientation depends on the handedness of the chiral molecules. These studies provide a new method for the miniaturization of ferromagnets using established synthetic protocols.

It has been recently observed that the application of a self-assembled chiral molecule monolayer on a magnetic layer can switch the direction of the perpendicularly magnetized substrate, and that the switching configurations depend on the handedness of the adsorbed molecules[55]. Here, enantiomers (chiral molecules) with different handedness are adsorbed on selected adsorption areas of the substrate. Chiral α-helix L-polyalanine or D-polyalanine and AHPA-L or AHPA-D oligopeptides are used as enantiomers in this experiment, where L and D denote left-handed and right-handed chiralities, respectively. Magnetic force microscopy is used to probe the orientation of the magnetization under the chiral molecules. The magnetic moments prefer to be aligned along the oligopeptide major axis for the AHPA-L (AHPA-D) region in the parallel (antiparallel) direction, and 10^{13} electrons per cm^2 are sufficient to induce magnetization reversal. These results present a new and efficient means to manipulate magnetization, which needs far fewer electrons by orders of magnitude than conventional STTs.

Finally, we note that chiral molecules can modify the superconducting order parameter, inducing spin-triplet pairing when interfaced with a conventional *s*-wave superconductor[56]. It has been known that superconductor/ferromagnet heterostructures can give rise to a novel spin-triplet pairing order parameter at interfaces, which has been intensively studied for potential applications in superconducting spintronics. However, this requires a non-trivial film growth technology to tune correlation length, transparency and the mean free path at the superconductor/ferromagnet interfaces, since the proximity effect is sensitive to the interfaces. On the other hand, simply by adsorbing chiral molecules on a superconductor, evidence of a chiral *p*-wave superconducting component with a triplet pairing symmetry has been observed from magnetotransport measurements on Nb films coupled to gold electrodes via polyalanine α-helix molecules and graphene flakes[57]. These results demonstrate that chirality can be transferred between different systems and can be utilized for spintronic devices. For example, coupling chiral molecules to a chiral antiferromagnetic material could enable simple reading and writing of the antiferromagnetic order.

Chiral magnetic nanostructures

Within the past decade, there has been tremendous interest in the fundamental properties of non-collinear chiral magnetic spin textures. Major classes of such spin textures include chiral domain walls in materials that exhibit perpendicular magnetic anisotropy and 2D or 3D magnetic nano-objects that have chiral non-collinear boundaries or surfaces. There has been an explosion in the number and type of these nano-objects, including skyrmions[58] and antiskyrmions[59], as well as merons[60], bimerons[61] and hopfions[62]. In all these cases, the chiral walls or boundaries can be Bloch-like or Néel-like, namely, the magnetization rotates (clockwise or anticlockwise) in a plane that is either tangential or perpendicular to the boundary, respectively. We use the term 'skyrmion' here to refer to the entire zoology of these nano-objects. Chiral domain walls and skyrmions can be manipulated or moved by spin currents via the SOTs that are generated from the interaction between these currents and the objects themselves. What is most interesting is that a series of chiral domain walls that alternate between boundaries between ↑|↓ and ↓|↑ magnetized domains. Here, | corresponds to a domain wall and can be moved all in the same direction by a spin current. This is only possible because each of the domain walls has the same chirality. This is the essence of chiral spintronics, that the chirality of spin-based phenomena or the chirality of the spin textures play a critical role in the properties of such systems.

Domain walls. Chiral SOTs manipulate chiral magnetic nanostructures in a significantly different way from conventional STTs[63,64]. As domain walls are topological excitations from a single domain ground state, they are topologically protected by certain symmetries. Indeed, the domain wall profile can be described by a topological soliton-like solution to the sine-Gordon equation[65,66] (Supplementary Information). This topological protection makes the use of domains as bits that encode information in memory and logic devices particularly useful, since the domain walls that separate the neighbouring domains are topologically robust. The governing exchange interaction in conventional collinear domain walls is the Heisenberg-type symmetric interaction. On the other hand, the chirality of a chiral domain wall is endowed typically by an additional antisymmetric exchange interaction, the DMI, that is observed in inversion symmetry broken systems, such as interfaces or in non-centrosymmetric bulk materials[58]. Of special note is an interface DMI (IDMI) that stabilizes Néel-type domain walls in perpendicularly magnetized thin films[67,68], although Néel-type chiral domain walls may be induced by bulk DMI in, for example, tetragonal ferrimagnetic layers[69]. Since a Bloch-type wall is

magnetostatically favourable in narrow domain walls, the IDMI induces an effective out-of-wall-plane local field, the IDMI field[63,70,71], such that the IDMI sign determines the chirality. For example, when IDMI is positive (right-handed chirality), the chiral domain walls are ↑ ← ↓ and ↓ → ↑ (FIG. 2a).

As mentioned above, the SOT[72,73] induced by the spin Hall effect[14,74] or the Rashba effect[13] is chiral, such that its handedness affects the direction of motion of chiral domain walls, as distinct from conventional STTs. For example, the right-handed (left-handed) SOT moves the right-handed (left-handed) chiral domain walls along the current flow direction, while the right-handed (left-handed) SOT drives the left-handed (right-handed) chiral domain walls along the electron flow direction. Here, note that the handedness of chiral Néel-type domain walls is constant, for a given DMI, irrespective of the domain wall configuration (↑|↓ or ↓|↑). Accordingly, the Néel domain wall magnetizations point in opposite directions between the two domain wall configurations (Supplementary Information). For example, ↑ ← ↓ and ↓ → ↑ are stabilized for a left-handed DMI chirality. Consequently, the domain wall velocity is identical for these two domain wall configurations for a given chirality of SOT and domain wall.

The degenerate dynamic states in chiral domain wall motion can be lifted by breaking symmetries, such as by applying an in-plane magnetic field perpendicular to the chiral axis of the domain walls (breaking time-reversal symmetry)[63,70], or by using geometrical twists, such as Y-shaped wires[75] or curved wires (breaking inversion symmetry)[76]. These broken symmetries can modify the strength and sign of the handedness of chiral domain walls, thereby, tuning the interactions of SOTs with chiral domain walls that depend on domain wall configurations. Note that the lifting of the degeneracy of the chiral interactions, either unintentionally or by design, can eliminate the information encoded within a sequence of domain walls. For example, possible unwanted slight extrusions or constrictions at wire edges during fabrication can act as a domain-wall-configuration-dependent pinning centre, thus, preventing the current-induced lockstep motion of multiple domain walls along such wires. Or, the curved regions in a wire that are designed to increase the chip density could erase the stored information when accessing bits. Antiferromagnetically coupled composite chiral domain walls in, for example, synthetic antiferromagnetic wires, can resolve this issue, as discussed below[75–77].

When chiral domain walls are formed between out-of-plane and in-plane magnetized domains, the

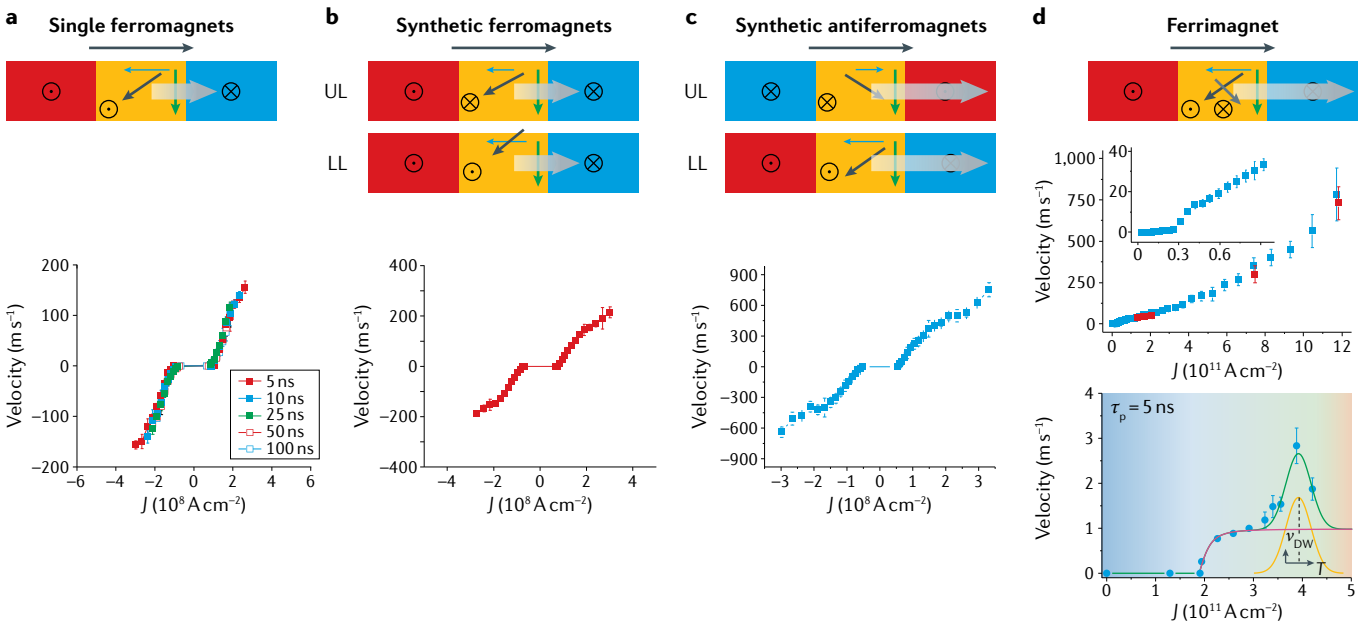

Fig. 2 | **Chiral magnetic domain wall motion by chiral spin–orbit torques.** Current-driven motion of chiral magnetic domain walls in a single ferromagnetic layer[63,64,70] (1.5 nm Pt/0.3 nm Co/0.7 nm Ni/0.15 nm Co; panel **a**), a ferromagnetically coupled bilayer across a spacer layer[19] (1.5 nm Pt/0.3 nm Co/0.7 nm Ni/0.15 nm Co/0.6 nm Ru/0.3 nm Co/0.7 nm Ni/0.15 nm Co; panel **b**), an antiferromagnetically coupled bilayer across a spacer layer[19] (1.5 nm Pt/0.3 nm Co/0.7 nm Ni/0.15 nm Co/0.8 nm Ru/0.15 nm Co/0.7 nm Ni/0.15 nm Co) (panel **c**) and a ferrimagnetic layer[81,82,160] (7 nm $Tm_3Fe_5O_{12}$/4 nm Pt (middle), 8 nm Pt/5 nm $Co_{76.7}Gd_{23.3}$ (bottom)) (panel **d**). Chiral domain wall motion by spin–orbit torque rotates the domain wall moment away from the Néel wall direction in perpendicularly magnetized wires and then the interfacial Dzyaloshinskii–Moriya fields generate an out-of-plane torque. This final torque moves the chiral domain walls. Note that the domain wall velocities for the two domain wall configurations are identical (the configuration-dependent domain wall velocity is not shown here but can be found in REF.[63]) (panel **a**). In a chiral composite domain wall that is formed when an exchange coupling interaction (ECI) couples two ferromagnetic layers, each containing a domain wall, the ECI induces a torque on each component chiral domain wall, an exchange coupling torque (ECT). The ECT direction in one component domain wall is opposite to the other, independent of the sign of the ECI. Hence, this torque is effective only for the antiferromagnetic coupling case (panel **c**), whilst it is zero for ferromagnetic coupling (panel **b**). Importantly, the ECT increases with the decreasing net magnetization. Since the ECI is typically large in ferrimagnets and bulk antiferromagnets, the ECT can be very large in these cases: nearly compensated ferrimagnetic insulator (middle) and ferrimagnetic metal (bottom) (panel **d**). LL, lower layer; UL, upper layer. Panel **a** adapted with permission from REF.[161], Copyright (2012) The Japan Society of Applied Physics. Panels **b** and **c** adapted with permission from REF.[19], Springer Nature Limited. Panel **d** adapted with permission from REFS[82,160], Springer Nature Limited.

Box 1 | **Role of chirality in injection and inversion of chiral domain walls by current**

Chirality can be used to devise a unique injector and an inverter of chiral domain walls compared with achiral counterparts. The baseline mechanism is to lower the Dzyaloshinskii–Moriya antisymmetric exchange interaction (DMI) energy, thereby, keeping the chirality that is given by the system, such as interfaces. Let us consider the left-handed chirality case here. Note that both the injector and the inverter require an in-plane magnetized region (a domain represented by either ⇒ or ⇐) that is artificially fabricated. This in-plane domain interfaces with neighbouring out-of-plane domains. The boundaries between them are chiral domain walls. When a current pulse is applied to this domain wall, a new domain wall can be created or not, which depends on the initial chirality of the domain wall. For example, when the domain wall was initially right-handed, a new domain wall is nucleated to switch it to the left-handed chirality and lower the DMI energy[16]. This is distinct from an achiral domain wall injection by the conventional spin transfer torque[162] (see the figure, panel **a**). For the inverter, when a chiral domain wall is injected to an in-plane domain region that is sandwiched by out-plane domains by a spin–orbit torque, the moment of the in-plane region is switched to lower the magnetic energy. This switching flips the domain wall into the right-handed chirality, thereby, increasing the DMI energy. To lower the DMI energy, a new domain wall is nucleated. The configuration of the new domain wall is opposite to the injected one, thereby, inverting the injected domain wall[17] (see the figure, panel **b**). Black solid and dashed rectangles highlight the left-handed and right-handed chiralities, respectively. The regions highlighted by solid rectangles (left-handedness) are in the low DMI energy state favoured by the interface DMI.

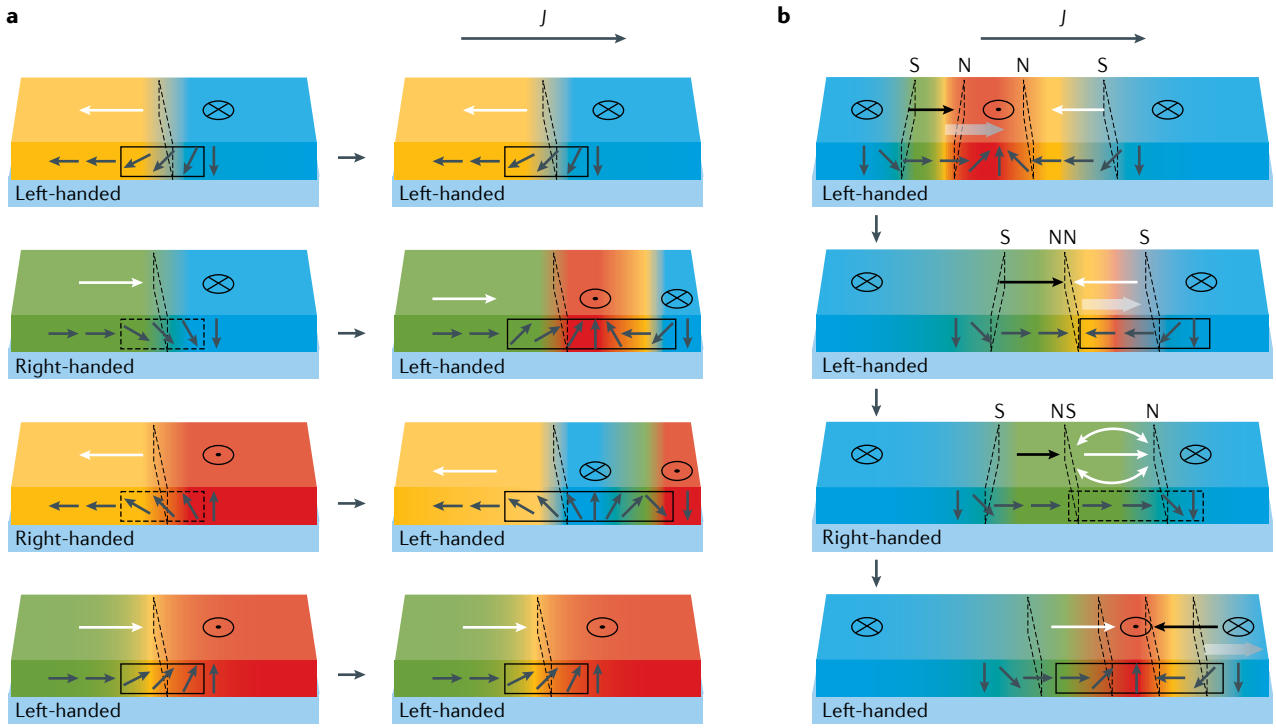

IDMI-induced local fields can be used to nucleate and manipulate domain walls (BOX 1). Like IDMI fields in chiral domain walls between oppositely magnetized domains, these fields are chiral and behave like switchable exchange bias fields. The direction of the fields is determined by the domain wall configuration and the sign of the IDMI. These effective fields can be used for field-free SOT switching, stabilization of skyrmions[15], chiral domain wall injectors[16] and inverters of chiral domain walls for logic applications. The interaction of a SOT with a chiral domain wall manifests itself as two useful functionalities: first, as a chiral domain wall injector that injects chiral domain walls from an in-plane region into an out-of-plane region[16], and, second, as a chiral domain wall inverter that consists of an artificially fabricated static chiral domain wall region (⇐) in a perpendicularly magnetized wire[17] (BOX 1). Note here that the in-plane region is artificially fabricated by, for example, exposure to oxygen. The baseline chirality set up by IDMI and in-plane|out-of-plane domain wall magnetization configurations determines whether a new chiral domain wall can be nucleated at the interface between the two regions. For example, when an initial state is in a DMI high energy state, a chiral domain wall can be nucleated to lower the energy, and vice versa, ending up with the chiral injection of domain wall. When the in-plane region is narrow, an injected chiral domain wall can be inverted by switching the magnetization in the in-plane region. These new findings can be useful to develop reconfigurable domain wall injectors and domain wall logic (BOX 1, panel **b**).

Composite domain walls. A composite domain wall can be formed from two chiral domain walls in two distinct magnetic layers that interact with one another via an antiferromagnetic exchange coupling across a thin, non-magnetic spacer layer[78]. The composite domain wall in the synthetic antiferromagnetic system (SAF) is also chiral and exhibits highly interesting interactions with spin currents[19,79,80]. The additional degrees of freedom and the antiferromagnetic exchange interaction gives rise to a novel torque, namely, an ECT, that moves such composite SAF domain walls much more efficiently

than the individual domain walls (FIG. 2c). The same ECT mechanism is also valid for ferrimagnets[81,82] and bulk antiferromagnets[83] (FIG. 2d). In addition, the degeneracy of the two domain wall configurations (↑|↓ in one layer and ↓|↑ in the second layer and the corresponding counterpart, namely, ↓|↑ in one layer and ↑|↓ in the other) in fully compensated SAFs is not lifted by external broken symmetries, such as longitudinal magnetic fields and curvature of racetrack devices[19,75,76]. These findings have established chiral SAF domain walls as highly promising candidates for the development of high-density and high-performance chiral spintronic memories and logic[77].

For small antiferromagnetic exchange coupling, the handedness of the component domain walls in a SAF may not be constant, but can oscillate when subjected to a SOT[20]. This happens when one of the component domain walls in the composite domain wall is subjected to a larger SOT than the other one (for the same current density) and when the two domain walls remain locked to each other via the antiferromagnetic exchange coupling (FIG. 3a). Consequently, the energy to move the composite domain wall is now used to precess one of the component domain walls and, thereby, dramatically slows the entire composite domain wall, whose velocity can go to zero (FIG. 3b,c). Thus, the composite domain wall velocity is the mean value of the sub-domain wall velocities weighted by the moments of the sub-domain walls. This is the exchange drag. Importantly, the domain wall structures can be destabilized when the drag exceeds a threshold value, such that the drag energy to move the slower sub-domain wall is converted to the precession or oscillation of sub-domain wall moments. This leads to a dramatic reduction of the composite domain wall velocity, the so-called exchange drag anomaly. In experiments, a large drag can be achieved using the chiral nature of domain walls by breaking time-reversal symmetry and lifting the domain wall degeneracy by applying an in-plane magnetic field[20] for the case of an uncompensated SAF (FIG. 3b). The chiral exchange drag is similar but distinct from other drag

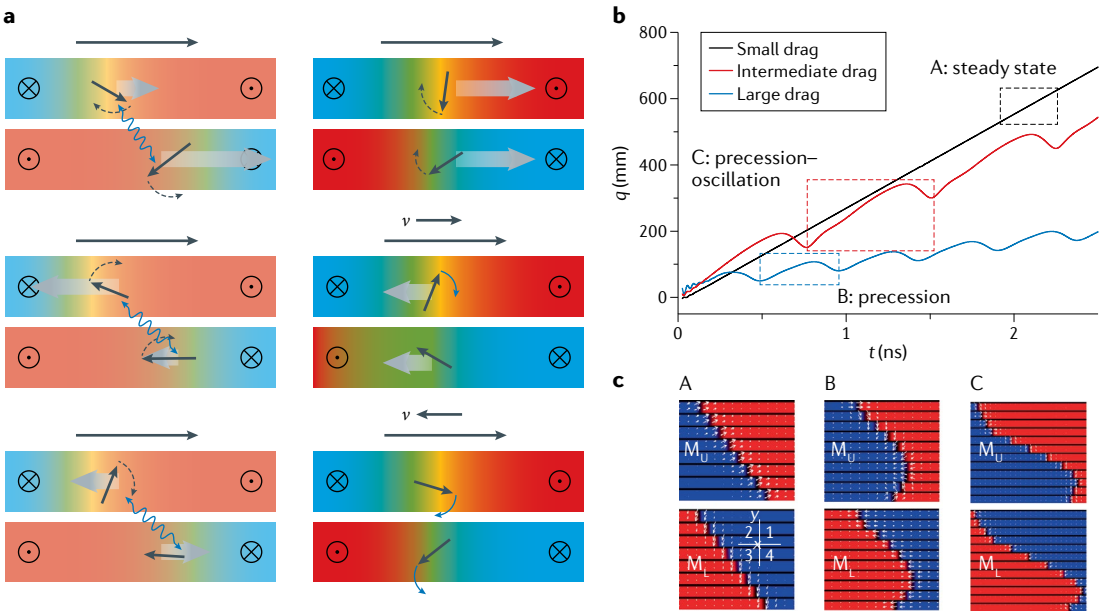

Fig. 3 | **Chiral exchange drag and chirality oscillation. a** | Schematic time-dependent snapshots of a synthetic antiferromagnet wire in the presence of a current pulse with current density *J*. The chiral exchange drag anomaly induces upper layer domain wall precession and lower layer domain wall oscillation. The left and right panels describe the domain wall dynamics for the position, unlocked (virtual) and locked (real), respectively. Note that the component domain walls are locked in the real world. The unlocked imaginary domain walls are introduced here to intuitively understand the drag mechanism A significantly larger spin–orbit torque induced by the longitudinal field is effective on the lower layer domain wall (↑↓) compared with the upper layer one (↓↑) (left). This large drag gives rise to the domain wall structural instability. Note that the composite domain wall position oscillates, while the sub-domain wall magnetizations precess/oscillate synchronously at typical ~GHz frequencies. This dramatically slows down the composite domain wall. **b** | Time-resolved evolution of the domain wall position, *q*, with varying drag strength. For small drag, the domain walls are stable, but as drag increases, the chiral exchange drag anomaly can be seen. **c** | Series of time-resolved 2D snapshots taken from micromagnetic simulations for three cases, indicated by the dashed squares in panel **b**. Successive snapshots are stacked vertically for the upper-layer and lower-layer magnetizations (M_U and M_L, respectively) in the synthetic antiferromagnetic system wire. Note that the domain wall positions are locked and coupled to each other in all three cases. The areas shown as red and blue colours correspond to ↑ and ↓ domains, respectively, thus, representing the out-of-plane components of the magnetizations. To display the in-plane components of the magnetizations, white arrows that represent the in-plane component of moments projected on the plane are shown. The four quadrants along with the *x* and *y* axes are displayed in the inset to panel **c**. The mean velocity of the composite chiral domain wall decreases with increasing drag, while the domain wall precession–oscillation frequency increases with increasing drag, since the energy to displace the composite chiral domain wall is used to precess or oscillate the domain wall magnetizations. Panels **b** and **c** adapted with permission from REF.[20], Springer Nature Limited.

Box 2 | **Topological Hall effect and skyrmion Hall effect**

When an electron travels in a crystal lattice with a Bravais lattice vector $\boldsymbol{a}$ and a periodic potential $V(\boldsymbol{r}+\boldsymbol{a})=v(\boldsymbol{r})$, such that the Hamiltonian $\mathcal{H}=\frac{p^2}{2m}+V(\boldsymbol{r})$, the electron wavefunction is described by a Bloch function

$$\psi_{\boldsymbol{k}}(\boldsymbol{r})=e^{i\boldsymbol{k}\cdot\boldsymbol{r}}u_{\boldsymbol{k}}(\boldsymbol{r}),$$

where $\boldsymbol{k}$, $\boldsymbol{r}$ and $u_k(\boldsymbol{r})$ are the crystal wave vector, spatial position and periodic function respectively, related by $u_{\boldsymbol{k}}(\boldsymbol{r}+\boldsymbol{a})=u_{\boldsymbol{k}}(\boldsymbol{r})$. Since the lattice periodic potential $v(\boldsymbol{r})$ acts as a periodically changing field to the moving electron, $|u_{\boldsymbol{k}}(t)=e^{-i\boldsymbol{k}\cdot\boldsymbol{r}}|\psi_{\boldsymbol{k}}(t)\rangle$ satisfies $i\hbar\frac{\partial}{\partial t}|u_{\boldsymbol{k}}(t)\rangle=\mathcal{H}(\boldsymbol{k},t)|u_{\boldsymbol{k}}(t)\rangle$ (REF.[163]), where $\mathcal{H}(\boldsymbol{k},t)=e^{-i\boldsymbol{k}\cdot\boldsymbol{r}}\mathcal{H}e^{i\boldsymbol{k}\cdot\boldsymbol{r}}$. If $|n(t)\rangle$ is an instantaneous eigenstate of $\mathcal{H}(\boldsymbol{k},t)$ at t with eigenvalue E_n, the velocity of the electrons

$$\boldsymbol{v}_n(\boldsymbol{k})=\frac{1}{\hbar}\left\langle\frac{\partial\mathcal{H}}{\partial\boldsymbol{k}}\right\rangle=\frac{1}{\hbar}\frac{\partial E_n}{\partial\boldsymbol{k}}-i\left(\left\langle\frac{\partial n}{\partial\boldsymbol{k}}\middle|\frac{\partial n}{\partial t}\right\rangle-\left\langle\frac{\partial n}{\partial t}\middle|\frac{\partial n}{\partial\boldsymbol{k}}\right\rangle\right)=\frac{1}{\hbar}\frac{\partial E_n}{\partial\boldsymbol{k}}-\frac{e}{\hbar}\boldsymbol{E}\times\boldsymbol{\Omega}_n(\boldsymbol{k}),$$

where the Lorentz force is given by $\frac{\partial\boldsymbol{k}}{\partial t}=-\frac{e}{\hbar}\boldsymbol{E}$ and the Berry curvature is given by $\boldsymbol{\Omega}_n(\boldsymbol{k})=i\langle\frac{\partial n}{\partial\boldsymbol{k}}|\times|\frac{\partial n}{\partial\boldsymbol{k}}\rangle$. Here, we find that $\boldsymbol{\Omega}_n(\boldsymbol{k})=\nabla\times\boldsymbol{A}_n(\boldsymbol{k})$, where $\boldsymbol{A}_n(\boldsymbol{k})=i\langle n|\frac{\partial n}{\partial\boldsymbol{k}}\rangle$ is the Berry connection. This shows that an electron that moves through a crystal lattice has an additional component of velocity, the anomalous velocity $-\frac{e}{\hbar}\boldsymbol{E}\times\boldsymbol{\Omega}_n(\boldsymbol{k})$, induced by the Berry curvature, which is the origin of the intrinsic spin Hall and intrinsic anomalous Hall effects. As an electron moves in a certain region subtended by surface $\boldsymbol{S}$ in the reciprocal space of the Brillouin zone, the electron feels the averaged transverse component of anomalous velocity, a solid angle $\gamma_n=\int_S d\boldsymbol{S}\cdot\boldsymbol{\Omega}_n$, the Berry phase.

This can be extended to the real-space case[97]. As an electron travels through a non-uniform periodic magnetic texture, skyrmion lattice here, the electron feels a time-varying magnetic field due to the magnetic texture. This field $\boldsymbol{B}(t)$ and its vector potential $\boldsymbol{A}(t)$ act as a Berry curvature $\boldsymbol{\Omega}(\boldsymbol{r})=i\langle\frac{\partial\boldsymbol{n}}{\partial\boldsymbol{x}}|\times|\frac{\partial\boldsymbol{n}}{\partial\boldsymbol{y}}\rangle$ and a Berry connection, respectively, thereby, inducing a transverse anomalous velocity and, consequently, a topological Hall effect (here, $\boldsymbol{n}=\boldsymbol{m}/|\boldsymbol{m}|$ and $\boldsymbol{m}$ is moment). The Berry phase $\gamma=\int d\boldsymbol{S}\cdot\boldsymbol{\Omega}=\int d^2r\boldsymbol{n}\cdot(\frac{\partial\boldsymbol{n}}{\partial\boldsymbol{x}}|\times|\frac{\partial\boldsymbol{n}}{\partial\boldsymbol{y}})$, is the net solid angle acquired by the electron during its travel through the skyrmionic magnetic texture, exactly corresponding to the topological charge (see the figure, panel **a**).

When skyrmions are driven by current, a similar anomalous velocity (or force) that moves the skyrmions transverse to the current direction can be induced, as seen in the topological Hall effect. This is termed the skyrmion Hall effect, which can be regarded as a reciprocal phenomenon of the topological Hall effect. The topological charge plays a key role in the skyrmion Hall effect, just as for the topological Hall effect. The equation of motion in the skyrmion centre of mass frame can be described by a Lorentz-like force equation with a topological charge under a dissipative force and Berry phase,

$$\mathcal{M}\ddot{\boldsymbol{R}}=-D\dot{\boldsymbol{R}}-\dot{\boldsymbol{R}}\times\boldsymbol{G}+\boldsymbol{F},$$

where $\mathcal{M}$ is the inertia of the skyrmion, $D=\frac{\alpha}{4\pi}\int d^2r\frac{\partial\boldsymbol{n}}{\partial x}\cdot\frac{\partial\boldsymbol{n}}{\partial y}$ is the dissipation tensor, $\boldsymbol{G}=(0,0,\frac{M}{\gamma}\int d^2r\boldsymbol{n}\cdot(\frac{\partial\boldsymbol{n}}{\partial\boldsymbol{x}}\times\frac{\partial\boldsymbol{n}}{\partial\boldsymbol{y}}))$ is the gyrocoupling vector that corresponds to the Berry phase (topological charge) and $\boldsymbol{F}$ is the external driving force to move the skyrmions, such as a spin transfer torque or a spin–orbit torque (α is the Gilbert damping, M is the magnetization and γ is the gyromagnetic ratio). The topological charge, skyrmion number, is composed of two factors: core polarization and winding number. Thus, the sign of the skyrmion Hall effect is determined by both the core polarization and the winding number (see the figure, panel **b**).

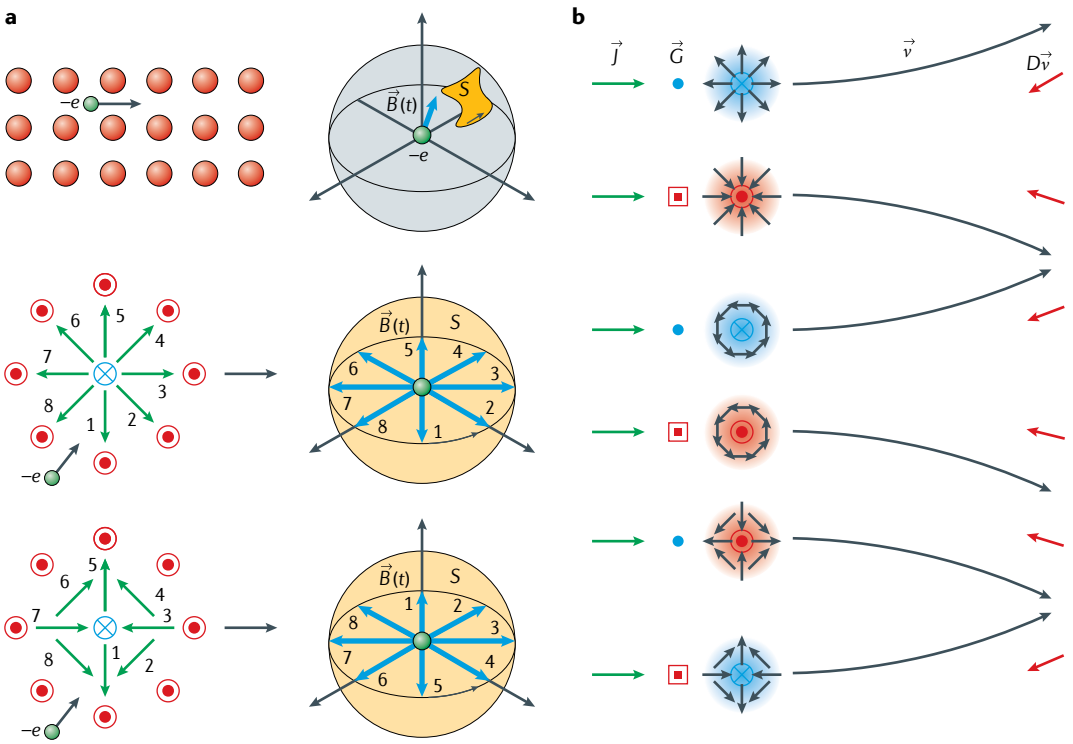

phenomena, such as Coulomb drag in coupled 2D electron gas systems, in which there is transfer only of linear momentum[84]. Interestingly, the oscillation frequency of the slower domain wall chirality is linearly proportional to the uncompensated moment of the SAF, thus, being analogous to massive Dirac fermions[85].

Skyrmions. In chiral skyrmions, swirling magnetic textures that are topologically non-trivial and which can be described by a non-zero topological charge, the skyrmion numbers[58,86] are potential information storage bits (BOX 2). Skyrmions and antiskyrmions have opposite winding numbers (skyrmion (+1) and antiskyrmion (−1)). An antiskyrmion is a more complex object than a skyrmion. Its boundary is composed of successive segments that alternate between Bloch-type and Néel-type walls with alternating chirality[59,87]. The stabilization of antiskyrmions in zero magnetic field and at room temperature is easier than for skyrmions due to the distinct symmetries of the DMI vectors that stabilize these objects in bulk materials. There has been significant progress in tuning phase stability[88], field history[89], exchange field[15], exchange-bias field[90], multi-stacking of films[91] and synthetic antiferromagnets[92].

Just as for chiral domain walls, IDMI favours Néel-type skyrmions, with a specific chirality that depends on the sign of the IDMI[93]. In contrast with chiral domain walls, the topological 2D nature of skyrmions gives rise to an additional component of torque that moves them transverse to the current direction, which is determined by the DMI or the IDMI, the skyrmion type (Néel or Bloch), Gilbert damping, the current direction (for the case of antiskyrmions) and the skyrmion number[94] (BOX 2, panel **b**). This so-called skyrmion Hall effect can be eliminated in ferrimagnets[95] and synthetic antiferromagnets[96], since two antiferromagnetically coupled lattices or layers display opposite skyrmion Hall effects that, thus, can cancel each other. Reciprocally, skyrmions apply a force transverse to moving spins, giving rise to an anomalous velocity of the spins perpendicular to the current flow direction. This force is solely topological, such that the spins feel like fictitious fields induced by acquisition of a Berry phase when they travel through a skyrmion or a lattice of skyrmions in real space; thus, the electrons display a topological Hall effect[97,98] (BOX 2, panel **a**).

Spin ice and spin liquids. The topological Hall effect can be observed in artificially fabricated chiral magnetic structures, such as an artificial chiral spin ice[99,100] that is a frustrated system of magnetic bars. The spin disorder resembles proton disorder in water ice, thereby, revealing the spin alignment of the bars and the magnetic frustration at the bar vertices[101]. When spins follow the chiral loop structure that forms at the edges of artificial chiral spin ice structures, the electrons acquire a Berry phase and an anomalous velocity in connected honeycomb structures[100]. Hence, the artificial chiral spin ice can be used as a sensitive probe of the spin chiral order parameter by detecting a net imbalance in either total chirality or its spatial distribution[102].

Unusual magnetotransport phenomena can be observed from topologically non-trivial chiral spin textures or non-collinear chiral antiferromagnets[103,104]. The interplay of such a novel magnetic structure with chiral spins can give rise to, for example, a large anomalous Hall effect[103,105] and a Nernst effect[106,107], even though the net magnetization is tiny. These phenomena arise from Berry curvatures from Bloch bands in momentum space near the Fermi level. The kagome lattices in the hexagonal structural forms of Mn_3X (X = Sn (REF.[103]), Ge (REF.[105]), Ir (REF.[108])) display a left-handed (negative) chirality of the Mn moments in a triangular lattice, since each Mn moment has its local easy-axis along the direction towards its in-plane nearest-neighbour X sites (FIG. 4a). Mn_3Sn is known to be a Weyl fermion metal, thus, showing a chiral anomaly. Recently, the chirality of the chiral antiferromagnet Mn_3Sn was shown to be switchable by what was claimed to be a SOT[109]. These materials have great potential for a chiral antiferromagnetic spintronic memory (FIG. 4b,c) that could have clear advantages from the absence of any significant long-range dipolar magnetic fields. In addition, non-collinear chiral antiferromagnets can serve as sources of chiral spin current and SOTs. Indeed, large charge-to-spin conversion efficiencies have been observed from the non-collinear antiferromagnet $Mn_3Ir(111)$ (REF.[108]), and an exotic form of spin Hall effect with unusual symmetry is exhibited from the non-collinear Mn_3Sn. Thus, evidence of spin Hall effect and inverse spin Hall effect arising from kagome lattices, what has been called a magnetic spin Hall effect[110], has been presented (FIG. 4c).

Another exotic chiral magnetic phase is a chiral spin liquid[111,112], in which a magnetic order is absent at the lowest temperatures due to frustrated exchange interactions and quantum fluctuations. In particular, spin liquids with a frustrated honeycomb lattice[113] exhibit a chiral spin liquid phase, in which time and parity symmetries are broken, whereas the lattice and spin rotation symmetries are not broken[114,115]. The chiral nature of this phase give rises to additional phenomena, such as an anomalous discontinuity in the magnetic torque[116] and a half-quantized thermal Hall effect[117], from the materials γ-Li_2IrO_3 (REF.[116]) and α-$RuCl_3$ (REF.[118]), respectively. Here, chiral edge currents of charge-neutral Majorana fermions that are topologically protected play a key role in the half-quantized thermal Hall effect in the presence of high magnetic fields that suppress long-range magnetic order[117]. Importantly, spin currents can be induced from spin-1/2 spinon excitations in 1D quantum-spin-chain-type spin liquids[119]. Spinon excitations are gapless, whereas the 1D quantum spin chain is a Heisenberg antiferromagnetic insulator, thus, exhibiting robustness against external magnetic fields and anisotropy, and a markedly long correlation length. Thus, the spin liquids have the potential to be used as spin current sources in insulator-based chiral spintronics.

Chiral topological quantum matter

Spinless chiral states in condensed matter physics have been observed as a quantum Hall effect in 2D systems that have a topologically non-trivial insulating phase in the bulk and chiral edge states under magnetic fields that break time-reversal symmetry[120]. In the chiral edge states, the Lorentz force dictates the momentum

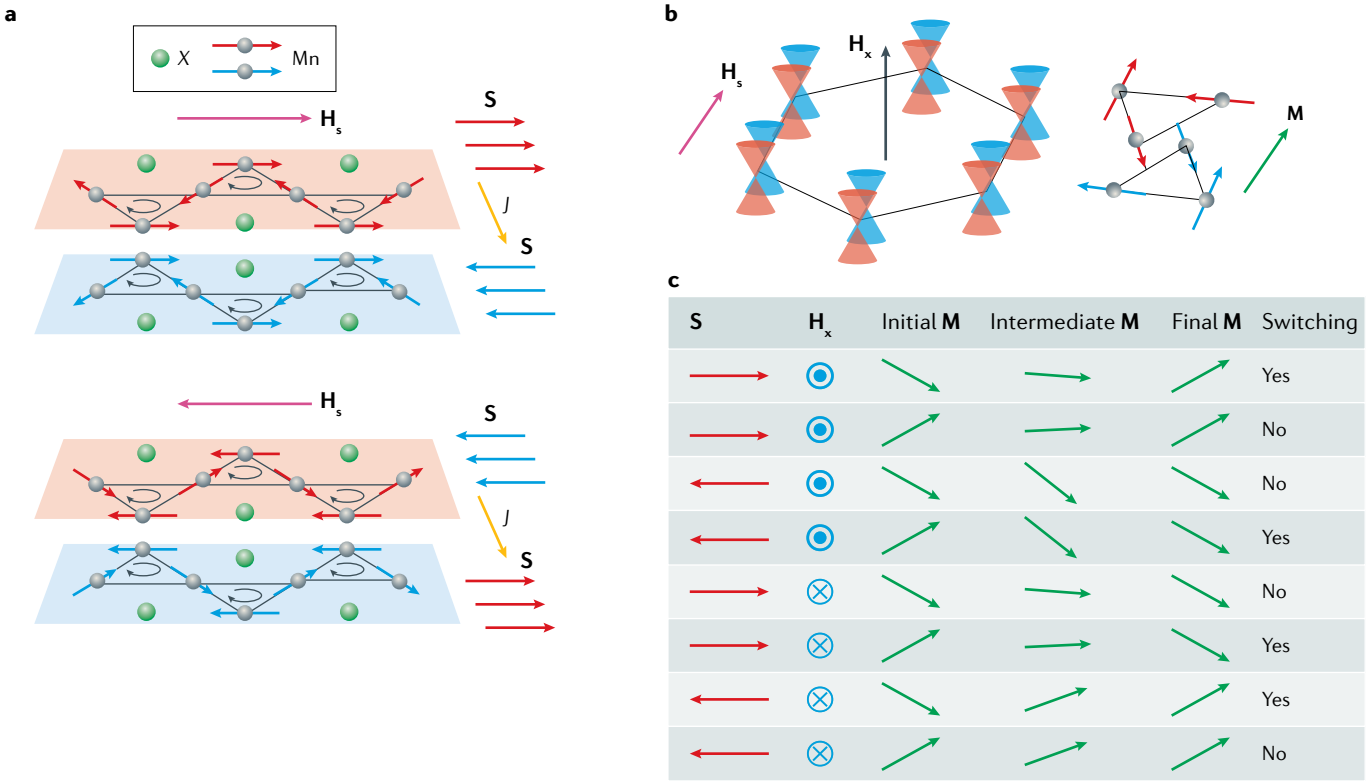

Fig. 4 | **Magnetotransport properties and chiral SOT-induced switching in chiral non-collinear antiferromagnets Mn_3X. a** | Mn_3X crystal structure and inverse triangular spin structure in the presence of a large magnetic field, $\mathbf{H_S}$, that switches and saturates the Mn moments. Note that the chirality of the Mn kagome lattice is left-handed (negative), which is conserved under the switching by $\mathbf{H_S}$. Large Berry curvature near the Fermi level due to Weyl fermionic behaviour induces a large anomalous Hall effect[103,105]. In the presence of an electric current *J*, the magnetic spin Hall effect induces a spin current in Mn_3X (REF.[110]). The accumulated spin polarization **S** induced by the spin current in Mn_3X is parallel to the magnetic octuple **M**. As distinct from the conventional spin Hall effect in non-magnetic metals, the magnetic spin Hall effect depends on the orientation of the magnetic octuple **M**, thus, showing a characteristic angular dependence. **b** | Schematic illustration of the Weyl points near the Fermi energy in momentum space[109]. Weyl nodes are close to the Fermi level (left), thereby, acting as both source and drain of Berry curvature that induces a large anomalous Hall effect. Note that the positions of the Weyl nodes change depending on the magnetic octuple **M**, that is, the saturation magnetic field $\mathbf{H_s}$ (right). **c** | In the presence of an external chiral spin–orbit torque (SOT) and small in-plane field $\mathbf{H_x}$, the magnetic octuple **M** can be switched, just like conventional SOT-induced switching of a perpendicularly magnetized moment. The chiral SOT applies a damping-like spin transfer torque on **M**, and then $\mathbf{H_x}$ applies a field-like torque on **M**, so, rotating and switching **M** deterministically, which can be detected by the anomalous Hall effect. The switching of **M** is determined by the current direction, the field direction and the initial direction of **M**, and the strength of anisotropy, as shown in the table.

direction, such that the spin-degenerate electrons move along only one edge for a given applied magnetic field and voltage. Later, it was realized that a SOI can play a similar role to the magnetic field, except for the important distinction that time-reversal symmetry is conserved in this case. The SOI locks spins to momenta in TIs and gives rise to spin currents along the edges. Consequently, the SOI causes spin currents to flow on opposite edges with opposite spin polarization and momentum[21,121]. Note that the SOI plays a similar role in inducing spin currents at the edges as for the chiral molecules. The induced edge states are helical — two copies of chiral states — thus, doubling the Hall conductance, to form the quantum spin Hall effect[122]. The quantum Hall effect and quantum spin Hall effect can be generalized to Chern insulators (broken time-reversal symmetry) and TIs (conserved time-reversal symmetry) that induce chiral and helical surface states, respectively, whereas the bulk is insulating (FIG. 5). TIs here denote a narrow meaning of TIs that have helical edge states, although there are many other types of what might be called TIs. With helical edge states, TIs can generate large spin currents, thus, serving as excellent building blocks and spin torque sources in chiral spintronics (FIG. 5b–d).

In TIs, the helical surface states induced by band inversion and large SOI near the Fermi level leads to spin-momentum locking[123,124] and associated phenomena, such as a large spin Hall effect[125] or a Rashba–Edelstein effect[126]. Although large spin currents at surfaces have been observed from TIs such as Bi_2Se_3 (REFS[125,127,128]), Bi–Sb (REFS[129,130]) and $(Bi,Te)_2Se_3$ (REF.[128]), care is required to quantify reliably the charge-to-spin conversion efficiency, which can be complicated by spurious effects[121] and a unidirectional magnetoresistance[131]. The low energy efficiency in SOTs from TIs may be challenging for practical applications at present due to the high resistivity, despite the high charge-to-spin conversion ratios[132].

Magnetic topological insulators. Intriguing quantum phenomena that are associated with the chiral nature of edge states emerge from magnetically doped TIs or intrinsically magnetic TIs[133]. This broken time-reversal

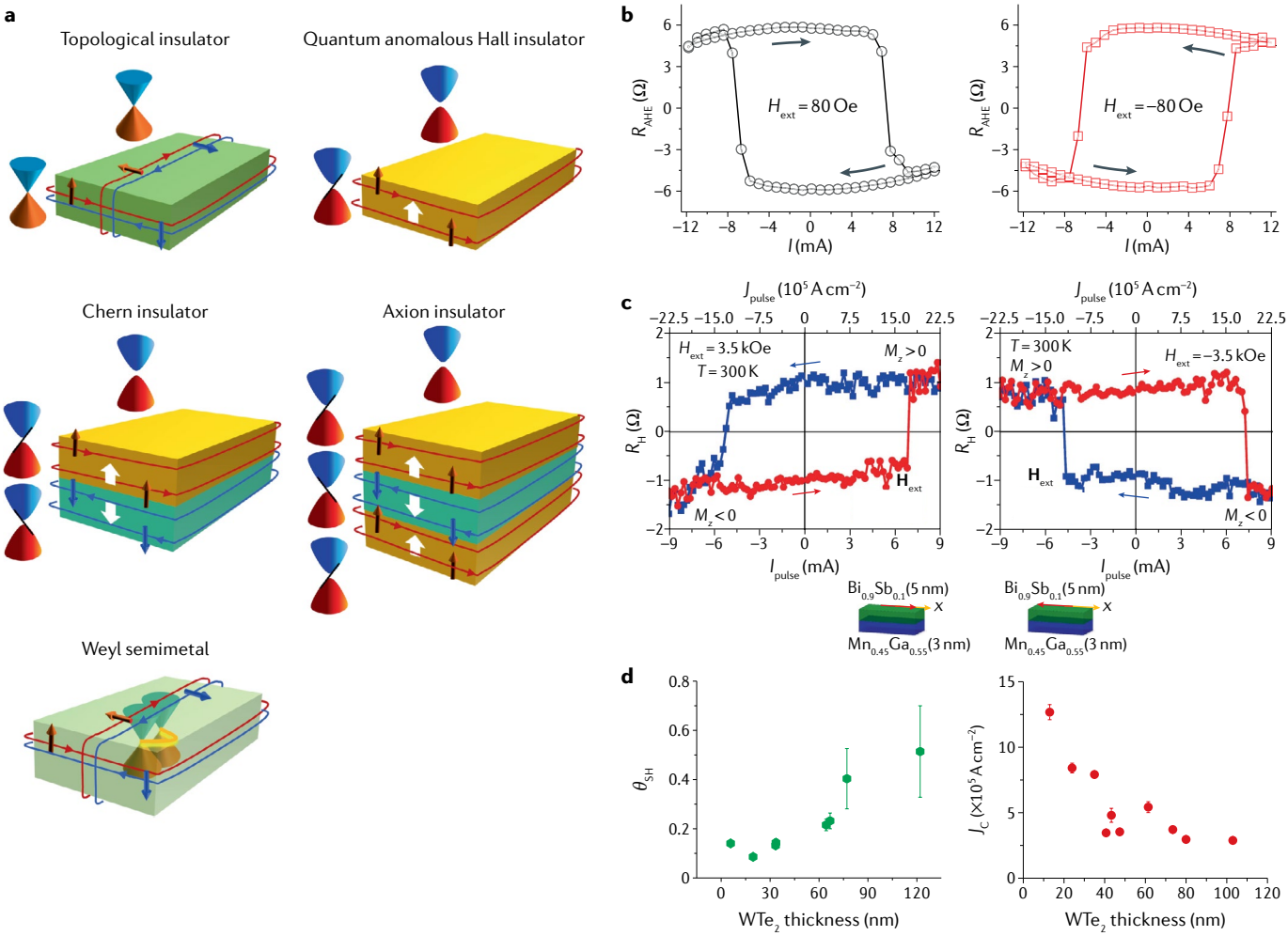

Fig. 5 | **Spin currents in chiral topological quantum materials, and spin–orbit torque from topological insulators and Weyl semimetals. a** | Schematic illustrations of the spin-polarized surface states of topological insulators, quantum anomalous Hall insulators, Chern insulators, axion insulators and Weyl semimetals. **b** | Current-induced switching of the magnetization due to a spin–orbit torque that arises from a $Bi_xSe_{(1-x)}$ underlayer in the presence of a constant 80 Oe (left) and −80 Oe (right) in-plane bias field. **c** | Room-temperature, current-induced magnetization switching of a $Bi_{0.9}Sb_{0.1}$(5 nm)/$Mn_{0.45}Ga_{0.55}$(3 nm) bilayer under an in-plane H_{ext} = +3.5 kOe (left) and H_{ext} = −3.5 kOe (right). **d** | The thickness-dependent charge-to-spin conversion efficiency of WTe_2 interfaced with $Ni_{81}Fe_{19}$ from a spin transfer torque ferromagnetic resonance measurement averaged between 6 and 7 GHz (left). WTe_2 thickness-dependent switching current density J_C in a WTe_2 layer (right). Panel **b** adapted with permission from REF.[127], Springer Nature Limited. Panel **c** adapted with permission from REF.[129], Springer Nature Limited. Panel **d** adapted with permission from REF.[146], Springer Nature Limited.

symmetry opens an exchange gap at the surfaces to which the magnetic moments are normal and splits the helical channels at the side surfaces into top and bottom chiral edges, which leads to a quantum anomalous Hall insulator or axion insulator, depending on the Chern number. Note that the Chern number is associated with the topological Berry phase (see Supplementary Information), such that a finite Chern number implies topologically non-trivial phases. The quantum anomalous Hall insulator exhibits quantized Hall resistance (h/e^2) and vanishing longitudinal resistance, as has been experimentally confirmed in Cr-doped $(Bi,Sb)_2Te_3$ (REF.[134]), V-doped $(Bi,Sb)_2Te_3$ (REF.[135]), modulation-doped Cr-$(Bi,Sb)_2Te_3$ (REF.[136]) and intrinsic $MnBi_2Te_4$ (REFS[137,138]) at low temperatures (FIG. 5a). $MnBi_2Te_4$ is particularly intriguing due to its 2D nature and the antiferromagnetic interlayer exchange coupling between successive ferromagnetic MnTe bilayers that are separated by quintuple layers of Bi_2Te_3. Depending on the number of septuple layers in thin lamellae formed by exfoliation, the material is either a quantum anomalous Hall insulator ($\mathcal{C}$ = ±1 Chern number, longitudinal resistivity $\rho_{xx} = 0$, Hall resistivity $\rho_{xy} = h/e^2$) near zero field for odd septuple layers, an axion insulator ($C = 0$, ρ_{xx} = finite, $\rho_{xy} = h/e^2$) at low fields for even septuple layers or a Chern insulator ($\mathcal{C}$ = ±1, $\rho_{xx} = 0$, $\rho_{xy} = h/e^2$) at high fields for even septuple layers[138] (FIG. 5a). In the axion insulating phase, the edge states cancel each other at the interfaces between antiferromagnetically aligned neighbouring layers (FIG. 5a). The axionic phase can reveal magnetoelectric effects[139] that may be useful for spintronic applications. Importantly, perfectly polarized spin currents in the quantum anomalous Hall edge states potentially provide a spin torque source, although the spin current density is limited by the quantum conductance (e^2/h).

The chiral nature of the edge states in magnetic TIs reveals additional interesting features — quantized conduction in magnetic domain walls, along which two chiral edge modes co-propagate[140], a large Rashba–Edelstein effect and a unidirectional magnetoresistance[141]. This allows the potential application of magnetic TIs for chiral topological spintronic applications, although the low Curie temperatures for magnetic TIs (up to 250 K at the highest doping level to date)[142] and the limited number of quantized spin current channels may be challenging for applications at room temperature. TI/magnetic layer heterostructures may be an alternative approach to obtain increased Curie temperatures[143].

Dirac and Weyl semimetals. Another class of chiral quantum matter in chiral spintronics are Dirac or Weyl semimetals that have Dirac and Weyl cones in the bulk, respectively, with nodes that are protected against hybridization by crystalline symmetry[23]. The topology of the bulk bands induces topological surface states and forms exotic Fermi arcs on the surface, as finite Chern numbers (which indicate topological non-triviality) exist only in the region between the Dirac or Weyl points[144]. In a Dirac semimetal, all bands are doubly degenerate, whereas in a Weyl semimetal, the degeneracy is lifted due to the breaking of the inversion or time-reversal symmetry or both, which is analogous to the TIs and magnetic TIs, as discussed above. Thus, a Dirac semimetal can be regarded as two copies of a Weyl semimetal. One of the most pronounced consequences of the chiral nature in a Weyl band structure is the chiral anomaly that populates Weyl fermions with a specific chirality, thus, giving rise to a chiral current and a characteristic negative magnetoresistance in the presence of parallel magnetic and electric fields[85], although extra care is needed to interpret the data to eliminate spurious effects[145]. Like TIs, the non-trivial Weyl band structures can generate large spin currents and SOTs due to the large Rashba–Edelstein effect that may be even larger than in TIs[146–148] (FIG. 5a).

Topological superconductors. A superconducting version of a TI is a topological superconductor that can be regarded as a TI with particle–hole symmetry[21]. Depending on whether time-reversal symmetry is broken, topological superconductors can be divided into helical (time-reversal symmetry unbroken) and chiral (time-reversal symmetry broken) cases, like TIs and magnetic TIs, respectively, as discussed above[149]. Particle–hole symmetry induces Majorana fermions from Dirac fermions in TIs by eliminating one degree of freedom. Since helical edge states in helical topological superconductors contain two copies of chiral edge states, chiral topological superconductors have chiral Majorana edge states with half the degree of freedom of chiral edge states in magnetic TIs. This gives rise to non-Abelian statistics that, thereby, has potential for applications in fault-tolerant topological quantum computation[150]. Similarly, a helical superconductor has helical Majorana edge states in which fermions with up spins are paired in the $p_x + ip_y$ state and fermions with down spins are paired in the $p_x - ip_y$ state, with half the degree of freedom of time-reversal symmetry invariant TI helical edge states. Note here that Majorana edge modes in topological superconductors can only support heat (chiral) or spin (helical) flow, since Cooper pairs do not carry heat and spin current in the superconducting state. Hence, a finite edge thermal or spin conductivity in a fully gapped topological superconductor can be a hallmark of dispersive Majorana fermions. Topological superconductors can be induced either intrinsically or artificially. For example, either odd-parity pairing or noncentrosymmetry with a strong spin-triplet component can lead to intrinsic topological superconductivity, such as the candidate materials Sr_2RuO_4 (REF.[151]), $Cu_xBi_2Se_3$ (REF.[152]) and (Sn,In)Te (REF.[153]), although there are debates as to the chiral *p*-wave symmetry of the superconducting order parameter in Sr_2RuO_4 (REF.[154]). Especially, topological superconductors with gapless bulk states like YPtBi (REF.[155]) may have the potential for chiral topological superconducting spintronics, since the topological superconductor surface has nodal lines that can induce helical Majorana fermions at the edges, thus, generating large spin currents. On the other hand, topological superconductors can be artificially engineered in hybrid systems consisting of a metal or semiconductor proximitized with a conventional *s*-wave superconductor, which can induce large chiral spin currents as well. An exotic chiral Majorana edge state can be formed from magnetic TIs (such as $MnBi_2Te_4$) in *s*-wave superconductor/magnetic TIs/*s*-wave superconductor Josephson junctions. Since the supercurrent in a Josephson junction corresponds to Andreev reflection and only chiral edge states are allowed in magnetic TIs, the supercurrent in the Josephson junction having magnetic TIs is carried by chiral Andreev edge states that have hybridized electron and hole states[156]. The chiral Andreev edge states have perfectly polarized spin currents, thereby, serving as useful spin torque sources for chiral superconducting spintronics.

Outlook

As modern electronics and spintronics have fundamentally changed our everyday lives, the association of chirality in moving spins is about to open the door to another opportunity, allowing the development of new means and methods. For example, chiral-molecule-based spintronics can reduce the spin injector size down to a single-molecule level, modifying the interface electronic structure that can alleviate Schottky barrier issues and switch magnetic field direction at interfaces without high currents. These features should be coupled to standard magnetic chiral devices. Yet, along with these advantages, there are still challenges. The main challenge is to combine and integrate the different parts of chiral spintronics into effective high speed and efficient devices. For example, using chiral molecules electric field can inject spin fast, but chirality itself changes slowly. This might be overcome by photoexcitation that induces isomerization through the excited molecules. Another challenge is to understand fully the CISS mechanism that would allow a further increase of spin selectivity in chiral molecules. More experimental data and active theoretical efforts will help understand the

true mechanism and physics. For example, theories should go beyond the single-electron picture and the D.C. linear regime, towards the multielectron transient nonlinear regime. The experiments should probe the CISS at the single-molecular level and explore the coherent quantum effects of spins in chiral molecules.

Chiral domain walls and skyrmions have several excellent figures of merit, including high efficiency against achiral counterparts for applications to memory, logic and memristic analogue devices[157]. Especially, coupled composite chiral domain walls and skyrmions in synthetic antiferromagnets and ferrimagnets are promising due to vanishing net moments and stray fields, large exchange couple torque, insensitivity to external fields or geometric effects, and exchange coupling fields to stabilize skyrmions at room temperature. In addition, chirality oscillation in weakly coupled chiral domain walls has the potential to produce radio frequency currents. However, there are still challenges for commercialization of chiral domain wall-based chiral spintronics, such as the reliable injection and propagation of domain wall by current pulses, reduction of current density, enhancement of thermal stability, electrical readout of bits encoded by domains and reduction of domain size. Ongoing enormous scientific and technological efforts will help overcome these challenges. Meanwhile, chiral domain walls in antiferromagnets can be used as a source of terahertz excitation of spin waves[158,159]. Especially, the laterally coupled chiral domain walls with in-plane regions have the potential to be used for electrical injection and inversion of chiral domain walls for injection of bits and logic operation in the future.

Non-collinear chiral antiferromagnets and chiral artificial spin ice can serve as either large spin current sources or memory bits, although the Hall voltages for readout have plenty of room for improvement to enable them to be used in memory applications. Especially, non-collinear chiral antiferromagnets have rich exotic properties that can be potentially used not only as SOT sources but storage bits as well. Likewise, chiral topological quantum matter such as TIs and Weyl semimetals can be useful for SOT-driven devices, since chiral/helical spin-momentum locked surface states are believed to generate large spin currents with a given charge current, although the low conductance compared with heavy metals needs to be considered. Chiral Majorana edge states from time-reversal symmetry broken topological superconductors are promising as sources of giant spin currents with zero conductance, thus, exhibiting effectively huge charge-to-spin conversion efficiency for SOT devices.

To overcome the difficulties discussed above and increase the potential of chiral spintronics, we believe that now is the time to merge chiral spintronics with all its branches, creating a simple device with advantages from each subfield.

Published online 8 April 2021

1. Linder, J. Improved domain-wall dynamics and magnonic torques using topological insulators. *Phys. Rev. B* **90**, 041412 (2014).
2. Yang, S.-H. Spintronics on chiral objects. *Appl. Phys. Lett.* **116**, 120502 (2020).
3. Banerjee-Ghosh, K. et al. Separation of enantiomers by their enantiospecific interaction with achiral magnetic substrates. *Science* **360**, 1331–1334 (2018).
An application of the CISS-induced exchange forces and the relevance of these forces to homochirality in life.
4. Naaman, R., Paltiel, Y. & Waldeck, D. H. Chiral molecules and the electron spin. *Nat. Rev. Chem.* **3**, 250–260 (2019).
5. Göhler, B. et al. Spin selectivity in electron transmission through self-assembled monolayers of double-stranded DNA. *Science* **331**, 894–897 (2011).
A demonstration of high spin selectivity of photoexcited electrons passing through chiral monolayers.
6. Yang, X., van der Wal, C. H. & van Wees, B. J. Spin-dependent electron transmission model for chiral molecules in mesoscopic devices. *Phys. Rev. B* **99**, 024418 (2019).
7. Naaman, R. & Waldeck, D. H. Comment on "Spin-dependent electron transmission model for chiral molecules in mesoscopic devices". *Phys. Rev. B* **101**, 026403 (2020).
8. Yang, X., van der Wal, C. H. & van Wees, B. J. Reply to "Comment on 'Spin-dependent electron transmission model for chiral molecules in mesoscopic devices'". *Phys. Rev. B* **101**, 026404 (2020).
9. Yang, X., van der Wal, C. H. & van Wees, B. J. Detecting chirality in two-terminal electronic nanodevices. *Nano Lett.* **20**, 6148–6154 (2020).
10. Nürenberg, D. & Zacharias, H. Evaluation of spin-flip scattering in chirality-induced spin selectivity using the Riccati equation. *Phys. Chem. Chem. Phys.* **21**, 3761–3770 (2019).
11. Dzyaloshinsky, I. A thermodynamic theory of "weak" ferromagnetism of antiferromagnetics. *J. Phys. Chem. Solids* **4**, 241–255 (1958).
12. Moriya, T. Anisotropic superexchange interaction and weak ferromagnetism. *Phys. Rev.* **120**, 91–98 (1960).
13. Manchon, A., Koo, H. C., Nitta, J., Frolov, S. M. & Duine, R. A. New perspectives for Rashba spin–orbit coupling. *Nat. Mater.* **14**, 871–882 (2015).
14. Sinova, J., Valenzuela, S. O., Wunderlich, J., Back, C. H. & Jungwirth, T. Spin Hall effects. *Rev. Mod. Phys.* **87**, 1213–1260 (2015).
15. Luo, Z. et al. Chirally coupled nanomagnets. *Science* **363**, 1435–1439 (2019).
16. Dao, T. P. et al. Chiral domain wall injector driven by spin–orbit torques. *Nano Lett.* **19**, 5930–5937 (2019).
17. Luo, Z. et al. Current-driven magnetic domain-wall logic. *Nature* **579**, 214–218 (2020).
18. Yang, S.-H. An all-electrical magnetic logic gate that harnesses chirality between domains. *Nature* **579**, 201–202 (2020).
19. Yang, S.-H., Ryu, K.-S. & Parkin, S. Domain-wall velocities of up to 750 m s^{-1} driven by exchange-coupling torque in synthetic antiferromagnets. *Nat. Nanotechnol.* **10**, 221–226 (2015).
This paper shows very efficient composite domain wall motion from antiferromagnets.
20. Yang, S.-H., Garg, C. & Parkin, S. S. P. Chiral exchange drag and chirality oscillations in synthetic antiferromagnets. *Nat. Phys.* **15**, 543–548 (2019).
Observation of chiral exchange drag and chirality oscillations from synthetic antiferromagnets.
21. Qi, X.-L. & Zhang, S.-C. Topological insulators and superconductors. *Rev. Mod. Phys.* **83**, 1057–1110 (2011).
22. Liu, C.-X., Zhang, S.-C. & Qi, X.-L. The quantum anomalous Hall effect: theory and experiment. *Annu. Rev. Condens. Matter Phys.* **7**, 301–321 (2016).
23. Armitage, N. P., Mele, E. J. & Vishwanath, A. Weyl and Dirac semimetals in three-dimensional solids. *Rev. Mod. Phys.* **90**, 015001 (2018).
24. Xie, Z. et al. Spin specific electron conduction through DNA oligomers. *Nano Lett.* **11**, 4652–4655 (2011).
25. Rosenberg, R. A., Mishra, D. & Naaman, R. Chiral selective chemistry induced by natural selection of spin-polarized electrons. *Angew. Chem. Int. Ed.* **54**, 7295–7298 (2015).
26. Kettner, M. et al. Spin filtering in electron transport through chiral oligopeptides. *J. Phys. Chem. C* **119**, 14542–14547 (2015).
27. Naaman, R. & Waldeck, D. H. Spintronics and chirality: spin selectivity in electron transport through chiral molecules. *Annu. Rev. Phys. Chem.* **66**, 263–281 (2015).
28. Suda, M. et al. Light-driven molecular switch for reconfigurable spin filters. *Nat. Commun.* **10**, 2455 (2019).
29. Yeganeh, S., Ratner, M. A., Medina, E. & Mujica, V. Chiral electron transport: scattering through helical potentials. *J. Chem. Phys.* **131**, 014707 (2009).
30. Medina, E., López, F., Ratner, M. A. & Mujica, V. Chiral molecular films as electron polarizers and polarization modulators. *EPL* **99**, 17006 (2012).
31. Liu, Y., Xiao, J., Koo, J. & Yan, B. Chirality-driven topological electronic structure of DNA-like materials. *Nat. Mater.* https://doi.org/10.1038/s41563-021-00924-5 (2021).
32. Gutierrez, R. et al. Modeling spin transport in helical fields: derivation of an effective low-dimensional Hamiltonian. *J. Phys. Chem. C* **117**, 22276–22284 (2013).
33. Michaeli, K., Beratan, D. N., Waldeck, D. H. & Naaman, R. Voltage-induced long-range coherent electron transfer through organic molecules. *Proc. Natl Acad. Sci. USA* **116**, 5931–5936 (2019).
34. Guo, A.-M. & Sun, Q. Spin-selective transport of electrons in DNA double helix. *Phys. Rev. Lett.* **108**, 218102 (2012).
35. Dalum, S. & Hedegård, P. Theory of chiral induced spin selectivity. *Nano Lett.* **19**, 5253–5259 (2019).
36. Michaeli, K., Varade, V., Naaman, R. & Waldeck, D. H. A new approach towards spintronics–spintronics with no magnets. *J. Phys. Condens. Matter* **29**, 103002 (2017).
37. Dor, O. B., Yochelis, S., Mathew, S. P., Naaman, R. & Paltiel, Y. A chiral-based magnetic memory device without a permanent magnet. *Nat. Commun.* **4**, 2256 (2013).
38. Aragonès, A. C. et al. Measuring the spin-polarization power of a single chiral molecule. *Small* **13**, 1602519 (2017).
39. Alam, K. M. & Pramanik, S. Spin filtering with poly-T wrapped single wall carbon nanotubes. *Nanoscale* **9**, 5155–5163 (2017).
40. Lu, H. et al. Spin-dependent charge transport through 2D chiral hybrid lead-iodide perovskites. *Sci. Adv.* **5**, eaay0571 (2019).
Close to 90% spin selectivity achieved in chiral perovskites crystals.

41. Bloom, B. P., Graff, B. M., Ghosh, S., Beratan, D. N. & Waldeck, D. H. Chirality control of electron transfer in quantum dot assemblies. *J. Am. Chem. Soc.* **139**, 9038–9043 (2017).
42. Mathew, S. P., Mondal, P. C., Moshe, H., Mastai, Y. & Naaman, R. Non-magnetic organic/inorganic spin injector at room temperature. *Appl. Phys. Lett.* **105**, 242408 (2014).
43. Abendroth, J. M. et al. Analyzing spin selectivity in DNA-mediated charge transfer via fluorescence microscopy. *ACS Nano* **11**, 7516–7526 (2017).
44. Ben Dor, O., Morali, N., Yochelis, S., Baczewski, L. T. & Paltiel, Y. Local light-induced magnetization using nanodots and chiral molecules. *Nano Lett.* **14**, 6042–6049 (2014).
45. Fontanesi, C., Capua, E., Paltiel, Y., Waldeck, D. H. & Naaman, R. Spin-dependent processes measured without a permanent magnet. *Adv. Mater.* **30**, 1707390 (2018).
46. Smolinsky, E. Z. B. et al. Electric field-controlled magnetization in GaAs/AlGaAs heterostructures–chiral organic molecules hybrids. *J. Phys. Chem. Lett.* **10**, 1139–1145 (2019).
47. Kumar, A., Capua, E., Fontanesi, C., Carmieli, R. & Naaman, R. Injection of spin-polarized electrons into a AlGaN/GaN device from an electrochemical cell: evidence for an extremely long spin lifetime. *ACS Nano* **12**, 3892–3897 (2018).
48. Eckshtain-Levi, M. et al. Cold denaturation induces inversion of dipole and spin transfer in chiral peptide monolayers. *Nat. Commun.* **7**, 10744 (2016).
49. Santos, J. I. et al. Chirality-induced electron spin polarization and enantiospecific response in solid-state cross-polarization nuclear magnetic resonance. *ACS Nano* **12**, 11426–11433 (2018).
50. Huang, Z. et al. Magneto-optical detection of photoinduced magnetism via chirality-induced spin selectivity in 2D chiral hybrid organic–inorganic perovskites. *ACS Nano* **14**, 10370–10375 (2020).
51. Inui, A. et al. Chirality-induced spin-polarized state of a chiral crystal $CrNb_3S_6$. *Phys. Rev. Lett.* **124**, 166602 (2020).
52. Koplovitz, G. et al. Magnetic nanoplatelet-based spin memory device operating at ambient temperatures. *Adv. Mater.* **29**, 1606748 (2017).
53. Al-Bustami, H. et al. Single nanoparticle magnetic spin memristor. *Small* **14**, 1801249 (2018).
54. Koplovitz, G. et al. Nano ferromagnetism: single domain 10 nm ferromagnetism imprinted on superparamagnetic nanoparticles using chiral molecules (Small 1/2019). *Small* **15**, 1970004 (2019).
55. Ben Dor, O. et al. Magnetization switching in ferromagnets by adsorbed chiral molecules without current or external magnetic field. *Nat. Commun.* **8**, 14567 (2017).
56. Alpern, H. et al. Unconventional superconductivity induced in Nb films by adsorbed chiral molecules. *New J. Phys.* **18**, 113048 (2016).
57. Sukenik, N. et al. Proximity effect through chiral molecules in Nb–graphene-based devices. *Adv. Mater. Technol.* **3**, 1700300 (2018).
58. Fert, A., Reyren, N. & Cros, V. Magnetic skyrmions: advances in physics and potential applications. *Nat. Rev. Mater.* **2**, 17031 (2017).
59. Nayak, A. K. et al. Magnetic antiskyrmions above room temperature in tetragonal Heusler materials. *Nature* **548**, 561–566 (2017).
60. Yu, X. Z. et al. Transformation between meron and skyrmion topological spin textures in a chiral magnet. *Nature* **564**, 95–98 (2018).
61. Shen, L. et al. Current-induced dynamics and chaos of antiferromagnetic bimerons. *Phys. Rev. Lett.* **124**, 037202 (2020).
62. Liu, Y., Hou, W., Han, X. & Zang, J. Three-dimensional dynamics of a magnetic hopfion driven by spin transfer torque. *Phys. Rev. Lett.* **124**, 127204 (2020).
63. Ryu, K.-S., Thomas, L., Yang, S.-H. & Parkin, S. Chiral spin torque at magnetic domain walls. *Nat. Nanotechnol.* **8**, 527–533 (2013).
64. Emori, S., Bauer, U., Ahn, S.-M., Martinez, E. & Beach, G. S. D. Current-driven dynamics of chiral ferromagnetic domain walls. *Nat. Mater.* **12**, 611–616 (2013).
These two papers present observations of chiral SOT from chiral domain walls.
65. Malozemoff, A. P. & Slonczewski, J. C. *Magnetic Domain Walls in Bubble Materials* (Elsevier, 1979).
66. Ezawa, Z. F. *Quantum Hall Effects* (World Scientific, 2013).
67. Thiaville, A., Rohart, S., Jué, É., Cros, V. & Fert, A. Dynamics of Dzyaloshinskii domain walls in ultrathin magnetic films. *EPL* **100**, 57002 (2012).
68. Garg, C. et al. Efficient chiral-domain-wall motion driven by spin-orbit torque in metastable platinum films. *Phys. Rev. Appl.* **14**, 034052 (2020).
69. Filippou, P. C. et al. Chiral domain wall motion in unit-cell thick perpendicularly magnetized Heusler films prepared by chemical templating. *Nat. Commun.* **9**, 4653 (2018).
70. Ryu, K.-S., Yang, S.-H., Thomas, L. & Parkin, S. S. P. Chiral spin torque arising from proximity-induced magnetization. *Nat. Commun.* **5**, 3910 (2014).
71. Yoshimura, Y. et al. Soliton-like magnetic domain wall motion induced by the interfacial Dzyaloshinskii–Moriya interaction. *Nat. Phys.* **12**, 157–161 (2016).
72. Miron, I. M. et al. Perpendicular switching of a single ferromagnetic layer induced by in-plane current injection. *Nature* **476**, 189–193 (2011).
Experimental observation of SOT.
73. Garello, K. et al. Symmetry and magnitude of spin–orbit torques in ferromagnetic heterostructures. *Nat. Nanotechnol.* **8**, 587–593 (2013).
74. Hoffmann, A. Spin Hall effects in metals. *IEEE Trans. Magn.* **49**, 5172–5193 (2013).
75. Garg, C. et al. Highly asymmetric chiral domain-wall velocities in Y-shaped junctions. *Nano Lett.* **18**, 1826–1830 (2018).
76. Garg, C., Yang, S.-H., Phung, T., Pushp, A. & Parkin, S. S. P. Dramatic influence of curvature of nanowire on chiral domain wall velocity. *Sci. Adv.* **3**, e1602804 (2017).
77. Parkin, S. & Yang, S.-H. Memory on the racetrack. *Nat. Nanotechnol.* **10**, 195–198 (2015).
78. Parkin, S. S. P., More, N. & Roche, K. P. Oscillations in exchange coupling and magnetoresistance in metallic superlattice structures: Co/Ru, Co/Cr, and Fe/Cr. *Phys. Rev. Lett.* **64**, 2304–2307 (1990).
79. Yang, S.-H. & Parkin, S. Novel domain wall dynamics in synthetic antiferromagnets. *J. Phys. Condens. Matter* **29**, 303001 (2017).
80. Cohen, A. et al. Current driven chiral domain wall motions in synthetic antiferromagnets with Co/Rh/Co. *J. Appl. Phys.* **128**, 053902 (2020).
81. Bläsing, R. et al. Exchange coupling torque in ferrimagnetic Co/Gd bilayer maximized near angular momentum compensation temperature. *Nat. Commun.* **9**, 4984 (2018).
82. Avci, C. O. et al. Interface-driven chiral magnetism and current-driven domain walls in insulating magnetic garnets. *Nat. Nanotechnol.* **14**, 561–566 (2019).
83. Shiino, T. et al. Antiferromagnetic domain wall motion driven by spin-orbit torques. *Phys. Rev. Lett.* **117**, 087203 (2016).
84. Narozhny, B. N. & Levchenko, A. Coulomb drag. *Rev. Mod. Phys.* **88**, 025003 (2016).
85. Nielsen, H. B. & Ninomiya, M. The Adler-Bell-Jackiw anomaly and Weyl fermions in a crystal. *Phys. Lett. B* **130**, 389–396 (1983).
86. Nagaosa, N. & Tokura, Y. Topological properties and dynamics of magnetic skyrmions. *Nat. Nanotechnol.* **8**, 899–911 (2013).
87. Hoffmann, M. et al. Antiskyrmions stabilized at interfaces by anisotropic Dzyaloshinskii-Moriya interactions. *Nat. Commun.* **8**, 308 (2017).
88. Lemesh, I. et al. Current-induced skyrmion generation through morphological thermal transitions in chiral ferromagnetic heterostructures. *Adv. Mater.* **30**, 1805461 (2018).
89. Duong, N. K. et al. Stabilizing zero-field skyrmions in Ir/Fe/Co/Pt thin film multilayers by magnetic history control. *Appl. Phys. Lett.* **114**, 072401 (2019).
90. Yu, G. et al. Room-temperature skyrmions in an antiferromagnet-based heterostructure. *Nano Lett.* **18**, 980–986 (2018).
91. Moreau-Luchaire, C. et al. Additive interfacial chiral interaction in multilayers for stabilization of small individual skyrmions at room temperature. *Nat. Nanotechnol.* **11**, 444–448 (2016).
92. Legrand, W. et al. Room-temperature stabilization of antiferromagnetic skyrmions in synthetic antiferromagnets. *Nat. Mater.* **19**, 34–42 (2020).
93. Heinze, S. et al. Spontaneous atomic-scale magnetic skyrmion lattice in two dimensions. *Nat. Phys.* **7**, 713–718 (2011).
94. Jiang, W. et al. Direct observation of the skyrmion Hall effect. *Nat. Phys.* **13**, 162–169 (2017).
Direct observation of the skyrmion Hall effect.
95. Hirata, Y. et al. Vanishing skyrmion Hall effect at the angular momentum compensation temperature of a ferrimagnet. *Nat. Nanotechnol.* **14**, 232–236 (2019).
96. Zhang, X., Zhou, Y. & Ezawa, M. Magnetic bilayer-skyrmions without skyrmion Hall effect. *Nat. Commun.* **7**, 10293 (2016).
97. Bruno, P., Dugaev, V. K. & Taillefumier, M. Topological Hall effect and Berry phase in magnetic nanostructures. *Phys. Rev. Lett.* **93**, 096806 (2004).
98. Kurumaji, T. et al. Skyrmion lattice with a giant topological Hall effect in a frustrated triangular-lattice magnet. *Science* **365**, 914–918 (2019).
99. Skjærvø, S. H., Marrows, C. H., Stamps, R. L. & Heyderman, L. J. Advances in artificial spin ice. *Nat. Rev. Phys.* **2**, 13–28 (2020).
100. Branford, W. R., Ladak, S., Read, D. E., Zeissler, K. & Cohen, L. F. Emerging chirality in artificial spin ice. *Science* **335**, 1597–1600 (2012).
101. Nisoli, C., Moessner, R. & Schiffer, P. Colloquium: Artificial spin ice: Designing and imaging magnetic frustration. *Rev. Mod. Phys.* **85**, 1473–1490 (2013).
102. Farhan, A. et al. Emergent magnetic monopole dynamics in macroscopically degenerate artificial spin ice. *Sci. Adv.* **5**, eaav6380 (2019).
103. Nakatsuji, S., Kiyohara, N. & Higo, T. Large anomalous Hall effect in a non-collinear antiferromagnet at room temperature. *Nature* **527**, 212–215 (2015).
Observation of large anomalous Hall effect from non-collinear antiferromagnets.
104. Ikhlas, M. et al. Large anomalous Nernst effect at room temperature in a chiral antiferromagnet. *Nat. Phys.* **13**, 1085–1090 (2017).
105. Nayak, A. K. et al. Large anomalous Hall effect driven by a nonvanishing Berry curvature in the noncolinear antiferromagnet Mn_3Ge. *Sci. Adv.* **2**, e1501870 (2016).
106. Nagaosa, N., Sinova, J., Onoda, S., MacDonald, A. H. & Ong, N. P. Anomalous Hall effect. *Rev. Mod. Phys.* **82**, 1539–1592 (2010).
107. Miyasato, T. et al. Crossover behavior of the anomalous Hall effect and anomalous Nernst effect in itinerant ferromagnets. *Phys. Rev. Lett.* **99**, 086602 (2007).
108. Zhang, W. et al. Giant facet-dependent spin-orbit torque and spin Hall conductivity in the triangular antiferromagnet $IrMn_3$. *Sci. Adv.* **2**, e1600759 (2016).
109. Tsai, H. et al. Electrical manipulation of a topological antiferromagnetic state. *Nature* **580**, 608–613 (2020).
110. Kimata, M. et al. Magnetic and magnetic inverse spin Hall effects in a non-collinear antiferromagnet. *Nature* **565**, 627–630 (2019).
111. Savary, L. & Balents, L. Quantum spin liquids: a review. *Rep. Prog. Phys.* **80**, 016502 (2016).
112. Takagi, H., Takayama, T., Jackeli, G., Khaliullin, G. & Nagler, S. E. Concept and realization of Kitaev quantum spin liquids. *Nat. Rev. Phys.* **1**, 264–280 (2019).
113. Kitaev, A. Anyons in an exactly solved model and beyond. *Ann. Phys.* **321**, 2–111 (2006).
114. Liu, Z.-X. & Normand, B. Dirac and chiral quantum spin liquids on the honeycomb lattice in a magnetic field. *Phys. Rev. Lett.* **120**, 187201 (2018).
115. Modic, K. A., Ramshaw, B. J., Shekhter, A. & Varma, C. M. Chiral spin order in some purported Kitaev spin-liquid compounds. *Phys. Rev. B* **98**, 205110 (2018).
116. Modic, K. A. et al. Robust spin correlations at high magnetic fields in the harmonic honeycomb iridates. *Nat. Commun.* **8**, 180 (2017).
117. Kasahara, Y. et al. Majorana quantization and half-integer thermal quantum Hall effect in a Kitaev spin liquid. *Nature* **559**, 227–231 (2018).
118. Cao, H. B. et al. Low-temperature crystal and magnetic structure of α-$RuCl_3$. *Phys. Rev. B* **93**, 134423 (2016).
119. Hirobe, D. et al. One-dimensional spinon spin currents. *Nat. Phys.* **13**, 30–34 (2017).
120. Klitzing, K. V., Dorda, G. & Pepper, M. New method for high-accuracy determination of the fine-structure constant based on quantized Hall resistance. *Phys. Rev. Lett.* **45**, 494–497 (1980).
121. Hasan, M. Z. & Kane, C. L. Colloquium: Topological insulators. *Rev. Mod. Phys.* **82**, 3045–3067 (2010).
122. Bernevig, B. A., Hughes, T. L. & Zhang, S.-C. Quantum spin Hall effect and topological phase transition in HgTe quantum wells. *Science* **314**, 1757–1761 (2006).
123. Fu, L. & Kane, C. L. Topological insulators with inversion symmetry. *Phys. Rev. B* **76**, 045302 (2007).
124. Zhang, H. et al. Topological insulators in Bi_2Se_3, Bi_2Te_3 and Sb_2Te_3 with a single Dirac cone on the surface. *Nat. Phys.* **5**, 438–442 (2009).
125. Mellnik, A. R. et al. Spin-transfer torque generated by a topological insulator. *Nature* **511**, 449–451 (2014).
Observation of chiral SOT from TI.
126. Rojas-Sánchez, J.-C. et al. Spin to charge conversion at room temperature by spin pumping into a new type of

topological insulator: α-Sn films. *Phys. Rev. Lett.* **116**, 096602 (2016).
127. Dc, M. et al. Room-temperature high spin–orbit torque due to quantum confinement in sputtered Bi_xSe_{1-x} films. *Nat. Mater.* **17**, 800–807 (2018).
128. Han, J. et al. Room-temperature spin-orbit torque switching induced by a topological insulator. *Phys. Rev. Lett.* **119**, 077702 (2017).
129. Khang, N. H. D., Ueda, Y. & Hai, P. N. A conductive topological insulator with large spin Hall effect for ultralow power spin–orbit torque switching. *Nat. Mater.* **17**, 808–813 (2018).
130. Chi, Z. et al. The spin Hall effect of Bi-Sb alloys driven by thermally excited Dirac-like electrons. *Sci. Adv.* **6**, eaay2324 (2020).
131. Yasuda, K. et al. Current-nonlinear Hall effect and spin-orbit torque magnetization switching in a magnetic topological insulator. *Phys. Rev. Lett.* **119**, 137204 (2017).
132. Zhu, L., Ralph, Daniel, C. & Buhrman, R. A. Highly efficient spin-current generation by the spin Hall effect in $Au_{1-x}Pt_x$. *Phys. Rev. Appl.* **10**, 031001 (2018).
133. Tokura, Y., Yasuda, K. & Tsukazaki, A. Magnetic topological insulators. *Nat. Rev. Phys.* **1**, 126–143 (2019).
134. Chang, C.-Z. et al. Experimental observation of the quantum anomalous Hall effect in a magnetic topological insulator. *Science* **340**, 167–170 (2013).
135. Chang, C.-Z. et al. High-precision realization of robust quantum anomalous Hall state in a hard ferromagnetic topological insulator. *Nat. Mater.* **14**, 473–477 (2015).
136. Mogi, M. et al. Magnetic modulation doping in topological insulators toward higher-temperature quantum anomalous Hall effect. *Appl. Phys. Lett.* **107**, 182401 (2015).
137. Deng, Y. et al. Quantum anomalous Hall effect in intrinsic magnetic topological insulator $MnBi_2Te_4$. *Science* **367**, 895–900 (2020).
138. Liu, C. et al. Robust axion insulator and Chern insulator phases in a two-dimensional antiferromagnetic topological insulator. *Nat. Mater.* **19**, 522–527 (2020).
139. Nenno, D. M., Garcia, C. A. C., Gooth, J., Felser, C. & Narang, P. Axion physics in condensed-matter systems. *Nat. Rev. Phys.* **2**, 682–696 (2020).
140. Liu, M. et al. Large discrete jumps observed in the transition between Chern states in a ferromagnetic topological insulator. *Sci. Adv.* **2**, e1600167 (2016).
141. Lv, Y. et al. Unidirectional spin-Hall and Rashba–Edelstein magnetoresistance in topological insulator-ferromagnet layer heterostructures. *Nat. Commun.* **9**, 111 (2018).
142. Gupta, S., Kanai, S., Matsukura, F. & Ohno, H. Magnetic and transport properties of Sb_2Te_3 doped with high concentration of Cr. *Appl. Phys. Express* **10**, 103001 (2017).
143. Ou, Y. et al. Enhancing the quantum anomalous Hall effect by magnetic codoping in a topological insulator. *Adv. Mater.* **30**, 1703062 (2018).
144. Wan, X., Turner, A. M., Vishwanath, A. & Savrasov, S. Y. Topological semimetal and Fermi-arc surface states in the electronic structure of pyrochlore iridates. *Phys. Rev. B* **83**, 205101 (2011).
145. Liang, S. et al. Experimental tests of the Chiral anomaly magnetoresistance in the Dirac-Weyl semimetals Na_3Bi and GdPtBi. *Phys. Rev. X* **8**, 031002 (2018).
146. Shi, S. et al. All-electric magnetization switching and Dzyaloshinskii–Moriya interaction in WTe_2/ferromagnet heterostructures. *Nat. Nanotechnol.* **14**, 945–949 (2019).
147. Johansson, A., Henk, J. & Mertig, I. Edelstein effect in Weyl semimetals. *Phys. Rev. B* **97**, 085417 (2018).
148. Li, P. et al. Spin-momentum locking and spin-orbit torques in magnetic nano-heterojunctions composed of Weyl semimetal WTe_2. *Nat. Commun.* **9**, 3990 (2018).
149. Sato, M. & Ando, Y. Topological superconductors: a review. *Rep. Prog. Phys.* **80**, 076501 (2017).
150. Nayak, C., Simon, S. H., Stern, A., Freedman, M. & Das Sarma, S. Non-Abelian anyons and topological quantum computation. *Rev. Mod. Phys.* **80**, 1083–1159 (2008).
151. Mackenzie, A. P. & Maeno, Y. The superconductivity of Sr_2RuO_4 and the physics of spin-triplet pairing. *Rev. Mod. Phys.* **75**, 657–712 (2003).
152. Sasaki, S. et al. Topological superconductivity in $Cu_xBi_2Se_3$. *Phys. Rev. Lett.* **107**, 217001 (2011).
153. Novak, M., Sasaki, S., Kriener, M., Segawa, K. & Ando, Y. Unusual nature of fully gapped superconductivity in In-doped SnTe. *Phys. Rev. B* **88**, 140502 (2013).
154. Pustogow, A. et al. Constraints on the superconducting order parameter in Sr_2RuO_4 from oxygen-17 nuclear magnetic resonance. *Nature* **574**, 72–75 (2019).
155. Meinert, M. Unconventional superconductivity in YPtBi and related topological semimetals. *Phys. Rev. Lett.* **116**, 137001 (2016).
156. Amet, F. et al. Supercurrent in the quantum Hall regime. *Science* **352**, 966–969 (2016).
157. Yang, S., Garg, C., Phung, T., Rettner, C. & Hughes, B. Spin-orbit torque driven one-bit magnetic racetrack devices — memory and neuromorphic applications. *Int. Symp. VLSI Technol. Syst. Appl.* https://doi.org/10.1109/VLSI-TSA.2019.8804677 (2019).
158. Kampfrath, T. et al. Coherent terahertz control of antiferromagnetic spin waves. *Nat. Photonics* **5**, 31–34 (2011).
159. Mashkovich, E. A. et al. Terahertz optomagnetism: nonlinear THz excitation of GHz spin waves in antiferromagnetic $FeBO_3$. *Phys. Rev. Lett.* **123**, 157202 (2019).
160. Cai, K. et al. Ultrafast and energy-efficient spin–orbit torque switching in compensated ferrimagnets. *Nat. Electron.* **3**, 37–42 (2020).
161. Ryu, K-.S, Thomas, L., Yang, S-.H, Parkin, S.S.P. Current induced tilting of domain walls in high velocity motion along perpendicularly magnetized micron-sized Co/Ni/Co racetracks. *Appl. Phys. Express* **5**, 093006 (2012).
162. Phung, T. et al. Highly efficient in-line magnetic domain wall injector. *Nano Lett.* **15**, 835–841 (2015).
163. Xiao, D., Chang, M.-C. & Niu, Q. Berry phase effects on electronic properties. *Rev. Mod. Phys.* **82**, 1959–2007 (2010).

Acknowledgements
S.S.P.P. acknowledges the European Research Council (ERC) under the European Union's Horizon 2020 research and innovation programme (grant agreement no. 670166) and the European Union's Horizon 2020 research and innovation programme under grant agreement no. 766566. R.N. and Y.P. acknowledges the partial support from US Department of Energy grant no. ER46430 and from the Israel Ministry of Science and Technology.

Author contributions
S.-H.Y. and S.S.P.P. conceived and proposed this Review. The authors contributed to all aspects of the article.

Competing interests
The authors declare no competing interests.

Peer review information
Nature Reviews Physics thanks Cui-Zu Chang and the other, anonymous, reviewers for their contribution to the peer review of this work.

Publisher's note
Springer Nature remains neutral with regard to jurisdictional claims in published maps and institutional affiliations.

Supplementary information
The online version contains supplementary material available at https://doi.org/10.1038/s42254-021-00302-9.